

# Quantitative transportomics identifies Kif5a as a major regulator of neurodegeneration

Sahil H Shah<sup>1,2,3\*†</sup>, Lucio M Schiapparelli<sup>2†‡</sup>, Yuanhui Ma<sup>4</sup>, Satoshi Yokota<sup>1</sup>, Melissa Atkins<sup>1</sup>, Xin Xia<sup>1</sup>, Evan G Cameron<sup>1</sup>, Thanh Huang<sup>5</sup>, Sarah Saturday<sup>2</sup>, Catalina B Sun<sup>1</sup>, Cara Knasel<sup>1</sup>, Seth Blackshaw<sup>5</sup>, John R Yates<sup>4</sup>, Hollis T Cline<sup>2</sup>, Jeffrey L Goldberg<sup>1</sup>

<sup>1</sup>Byers Eye Institute and Spencer Center for Vision Research, Stanford University, Palo Alto, United States; <sup>2</sup>Scripps Research, Neuroscience Department and the Dorris Neuroscience Center, La Jolla, United States; <sup>3</sup>Neuroscience Graduate Program and Medical Scientist Training Program, University of California, San Diego, La Jolla, United States; <sup>4</sup>Scripps Research, Department of Molecular Medicine, La Jolla, United States; <sup>5</sup>Department of Neuroscience, Johns Hopkins University School of Medicine, Baltimore, United States

\*For correspondence: sahilshah90@gmail.com

†These authors contributed equally to this work

Present address: †The Department of Cell Biology, Duke University Medical School, Durham, United States

Competing interest: The authors declare that no competing interests exist.

Funding: See page 22

Received: 05 March 2021

Accepted: 07 March 2022

Published: 08 March 2022

Reviewing Editor: Paola Bovolenta, CSIC-UAM, Spain

© Copyright Shah et al. This article is distributed under the terms of the [Creative Commons Attribution License](https://creativecommons.org/licenses/by/4.0/), which permits unrestricted use and redistribution provided that the original author and source are credited.

**Abstract** Many neurons in the adult central nervous system, including retinal ganglion cells (RGCs), degenerate and die after injury. Early axon protein and organelle trafficking failure is a key component in many neurodegenerative disorders yet changes to axoplasmic transport in disease models have not been quantified. We analyzed early changes in the protein ‘transportome’ from RGC somas to their axons after optic nerve injury and identified transport failure of an anterograde motor protein Kif5a early in RGC degeneration. We demonstrated that manipulating Kif5a expression affects anterograde mitochondrial trafficking in RGCs and characterized axon transport in Kif5a knockout mice to identify proteins whose axon localization was Kif5a-dependent. Finally, we found that knockout of Kif5a in RGCs resulted in progressive RGC degeneration in the absence of injury. Together with expression data localizing Kif5a to human RGCs, these data identify Kif5a transport failure as a cause of RGC neurodegeneration and point to a mechanism for future therapeutics.

## Editor's evaluation

This study uses unbiased proteomics to determine which proteins are transported along the axon transportome in the context of optic nerve injury. Kif5a is identified as the most significantly down-regulated protein in the transportome after injury. Knocking out Kif5a resulted in degeneration of the axon, suggesting that Kif5a is crucial for maintaining a healthy optic nerve. Further, optic nerve analyses of the Kif5a KO vs the control upon injury identified defective mitochondrial transport and defective hRNP transport that has been identified as a cause of neurodegeneration in ALS upper motor neurons.

## Introduction

Adult mammalian central nervous system neurons often undergo cell death and axon degeneration after injury and in disease. Neurodegenerative diseases such as glaucoma and acute injuries such as after optic nerve trauma may result in irreversible retinal ganglion cell (RGC) loss. Mechanisms underlying this degeneration include intracellular events such as acute calcium influx into the axon

(Knöferle et al., 2010), loss of constitutive axon survival factors like Nmnat2 (Gilley et al., 2015), inhibition of trophic survival and growth pathways, as with suppressors of cytokine signaling (e.g. Socs3) and ciliary neurotrophic factor (CNTF) signaling or Dusp14 and mitogen-activated protein kinases (Cai et al., 1999; Zhou et al., 2005; Leaver et al., 2006; Park et al., 2010; Galvao et al., 2018), and neuron-extrinsic degenerative signaling, such as from reactive astrocytes (Liddelow et al., 2017) and microglia. Major strides in understanding neurodegeneration in neurons including RGCs have been made in recent years, including transcriptomic (Yasuda et al., 2016), proteomic (Belin et al., 2015), and metabolomic (Sato et al., 2018) cellular changes.

Axon transport failure has been pathophysiologically linked to RGC death in glaucoma, as well as to other neurodegenerative diseases such as amyotrophic lateral sclerosis (ALS) and Alzheimer's disease (Zhang et al., 2004; Nicolas et al., 2018). While changes described in transcriptional and gene-regulatory networks in neurons can be a proxy for changes in a neuron's or an axon's molecular components, it does not capture dynamics in expression or localization of proteins. Proteomics experiments in RGC somas have identified axon injury-induced pathways (Belin et al., 2015), but it is not known how molecular trafficking to the damaged optic nerve changes after injury. Unbiased temporal and spatial quantification of protein transport in vivo has presented technical challenges, including the overall low proportion of transported proteins, and the need to purify target axon proteins from surrounding mixed cellular populations.

We previously developed a mass spectrometry-compatible technique for characterizing the axon transportome in the visual system (Schiapparelli et al., 2019). Here, we adapt this technique to quantify changes in the axon transportome after optic nerve injury. We identify transport failure of a kinesin-1 motor protein, Kif5a, which we find expressed in human RGCs and also implicated in genetics of neurodegeneration outside the visual system (Tessa et al., 2008; Nicolas et al., 2018). We use transportome proteomics to identify proteins whose transport is dependent on Kif5a, and finally we validate the importance of Kif5a for adult RGC survival in vivo. Together this study adapts novel methods to identify Kif5a transport deficits as a contributor to RGC death after injury and offers new insights into kinesin motor cargo specificity.

## Results

### Pulsed NHS-biotin labels proteins for differential immunofluorescence and proteomics

After optic nerve crush in rats, 65% of RGCs die within 1 week, while less than 1% die after 1 day (Sánchez-Migallón et al., 2016). We were interested in identifying potential differences in axonally transported proteins after axon damage, but before cell death. In previous studies we used repeated daily intravitreal injections of *N*-hydroxysuccinimidobiotin (NHS-biotin) over a week in adult rats for steady-state mass spectrometry-based quantification of anterogradely transported proteins in the optic nerve (Schiapparelli et al., 2014; Schiapparelli et al., 2019). NHS-biotin covalently binds primary amines on proteins, principally lysines and N-terminal amino acids, adding a biotin group (Figure 1a), which is identifiable by the specific shift in peptide molecular weight in mass spectrometry or by immunodetection. Here, we adapted our NHS-biotin protocol to a 24 hr window to provide improved temporal resolution, favoring it over two alternative methods tested (Figure 1—figure supplement 1), consistent with our goal to study early changes after optic nerve crush. Animals received two intravitreal injections, the first at the same time as optic nerve crush or sham surgery and a second 21 hr later, 3 hr before tissue collection, to capture both fast and slow axon transport. Although a variety of retinal proteins are labeled by intravitreal injection, dissection of the optic nerve isolates only proteins which have been transported from RGC somas into RGC axons (Figure 1b). Biotinylated, transported proteins were visualized with tyramide signal amplification in the control optic nerve and region of the injured optic nerve proximal to the crush site (Figure 1c). Notably, there was no biotin signal distal to the crush, confirming the disruption of protein transport and lack of biotin transfer out of axons after injury. Together these data indicate that this protocol results in protein labeling within RGC axons in the optic nerves in both the control and injury conditions, allowing targeted isolation and investigation of changes in RGC proteins transported into the optic nerve after injury.

We used tandem mass spectrometry (MS/MS) combined with direct detection of biotin-containing tags enrichment to selectively isolate and identify biotinylated peptides. Directly measuring biotin

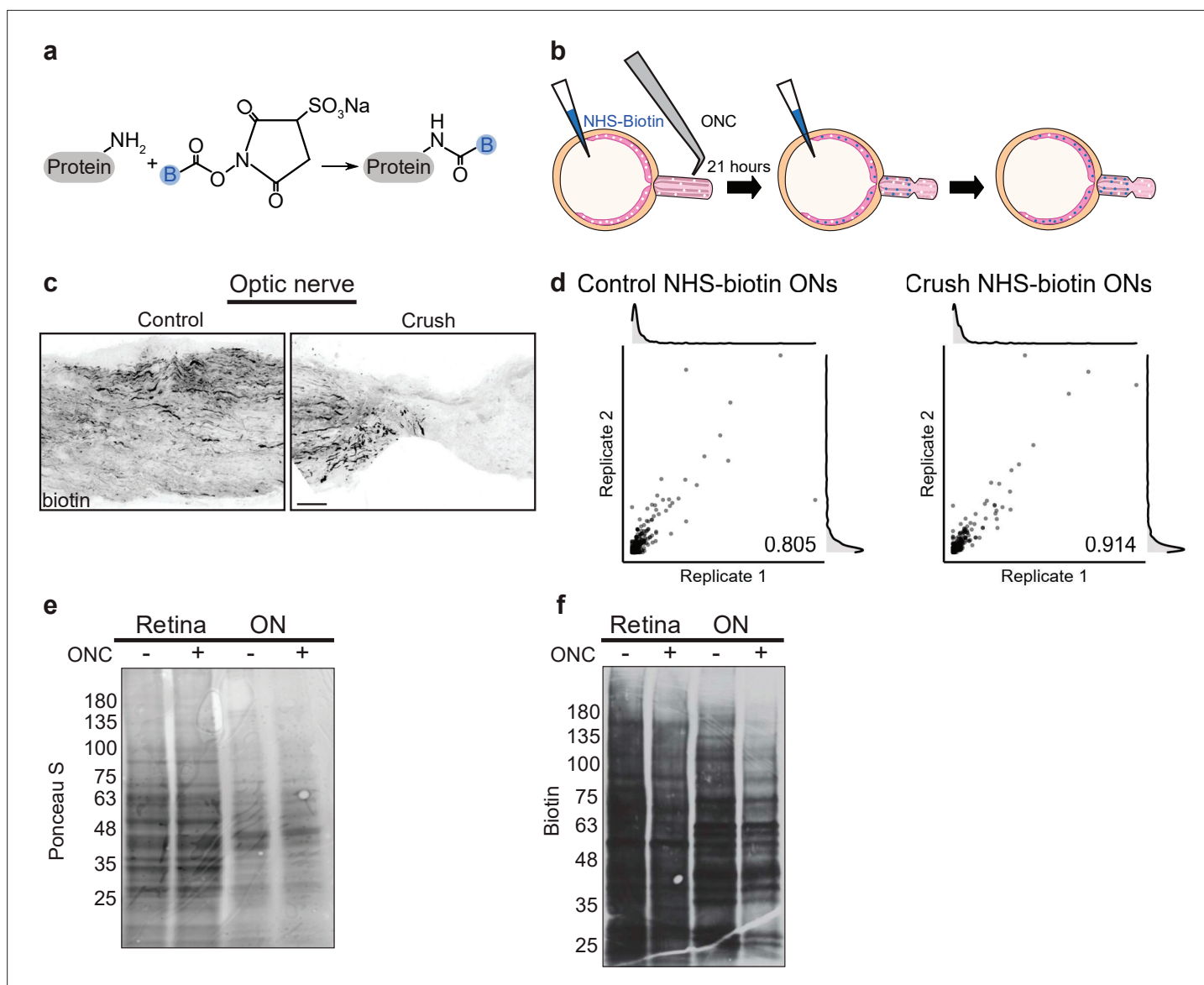


**Figure 1.** Pulsed *N*-hydroxysuccinimidobiotin (NHS-biotin) labels and quantifies protein transport after injury. **(a)** NHS-biotin (biotin group in blue) reacts with primary amines adding a defined mass shift to tagged proteins. **(b)** NHS-biotin (blue) was injected before injury with a repeat injection 21 hr later. Biotinylated proteins in retinal ganglion cells (RGCs) transport down intact RGC axons in the optic nerve. The retinas and optic nerves were collected for tissue processing after 3 hr. **(c)** No biotinylated proteins were detected by immunofluorescence distal to the crush site. Scale bar, 100 μm. **(d)** Pearson's R correlation of proteomic replicates of control or optic nerve crush (ONC) samples ( $R = 0.805$  and  $0.914$ , respectively). **(e)** Ponceau S stain of protein from biotinylated retinas and optic nerves, with and without ONC, showing equivalent total protein. Molecular ladder labeled on left of blot. **(f)** Western blot of the same samples run in parallel, probing for biotin. ONC decreased biotinylated proteins to a greater extent in ON compared to retina. Molecular ladder labeled on left of blot.

The online version of this article includes the following source data and figure supplement(s) for figure 1:

**Source data 1.** Proteomic quantification of transportome changes after ONC from **Figure 1b**.

**Source data 2.** Raw western blots from **Figure 1**.

**Figure supplement 1.** Alternative protein labeling strategies.

**Figure supplement 1—source data 1.** Raw western blots from **Figure 1—figure supplement 1**.

mass shifts on lysine residues in peptides with MS/MS facilitates direct quantification of biotinylated proteins with improved specificity (*Schiapparelli et al., 2014*). To minimize variability and increase protein yield, we combined eight optic nerves of either control or injury conditions for each MS sample. During dissection, we included optic nerve fragments from the end of the orbit to the chiasm from both injured and sham operated samples to ensure comparable tissue processing. A total of six samples, three each of control or optic nerve crush, were run independently through MS/MS. We detected 206–300 transported proteins with a range of detection of expression up to 300-fold normalized spectral abundance factor (NSAF) values. To assess reproducibility of the quantitative proteomics in each of these conditions, we used pairwise correlation of NSAF values which showed high correlation between replicates of both control and crush samples (**Figure 1d**,  $R = 0.805$  and  $R = 0.914$ , respectively). These experiments show that reducing the labeling window to 24 hr and comparing changes in NSAF values allow relative quantification between two conditions with high correlation between replicates, even in this tight temporal window before widespread apoptosis after optic nerve injury.

### Quantitative transportomics identifies specific proteins whose transport differs after injury

To ask whether protein transport into the optic nerve changed after injury, we measured the total protein abundance in control and injured retinas and optic nerve by electrophoresis, western blotting, and Ponceau S membrane staining. Total protein content was equivalent in optic nerve crush and control retinas and optic nerves, as expected given the short time between injury and tissue collection (**Figure 1e**). However, when we compared the biotinylated portion of total protein in crush or control conditions, we found a decrease in axon-transported protein after injury (**Figure 1f**), consistent with previous studies of total transport after injury (*Quigley et al., 1979; McKerracher et al., 1990*).

To test transport changes of individual proteins, we probed for Sncb, Gap43, and Arf3, neuronal proteins known to be transported down the optic nerve (*Leon et al., 2000; Schiapparelli et al., 2019; Figure 2a*). Four rat optic nerves were labeled and homogenized using the same protocol as above for proteomics, and then biotin-tagged proteins were immunoprecipitated with neutravidin-bound agarose beads. We compared retinal and optic nerve total proteins (input), as well as the biotinylated fraction pulled down by immunoprecipitation (IP), with and without injury. In the retina, there was little to no change in total protein levels (input, **Figure 2a**) or in the biotinylated fraction (IP, **Figure 2a**) in any of the three proteins, suggesting the abundance of these proteins is equivalent in the retinal cell bodies at this early time point after optic nerve injury. Sncb and Arf3 but not Gap43 showed significant decreases in transport into the optic nerve after injury (IP + vs. – crush, **Figure 2a**), and this decrease was significant even when normalizing to the decrease in total transported protein as captured in **Figure 1f** (normalized  $\log_2FC = -2.2$  for Sncb,  $-1.3$  for Arf3,  $n = 3$ ). This suggests that deficits in transport of specific proteins occur within the first 24 hr after optic nerve injury before changes in total protein can be detected. These data exemplify the need for axon-specific, temporally restricted protein labeling to accurately assess early axon transportome changes in the degenerative process.

We then examined the transportome changes after optic nerve crush using mass spectrometry. We normalized relative abundance of detected proteins within each condition to determine whether specific proteins are transported down the axon in greater or lesser amount relative to the global transport rate, which was decreased. Individual protein transport was quantified using NSAF in injured or control conditions across three replicates containing eight optic nerves each (complete data in **Figure 1—source data 1**). The relative log-normalized fold change of anterogradely transported proteins from RGC bodies to their axons in the optic nerve was visualized on a volcano plot (**Figure 2b**). Because mass spectrometry undersamples the total proteome and thus we did not want to filter too stringently, we analyzed proteins that had a  $\log_2$  fold change of greater than 1.5 of relative abundance in the transportome, or a p-value  $< 0.05$ , or both. This identified several proteins that fell into three ontologies of identified function: cytoskeletal (Tmsbx, Tcp1, Tuba1a, Tuba1b, Tuba3a, Nefl, and Ina), protein synthesis (Impact), and protein transport (Kif5a). In the protein transport ontology, transport of Kif5a, a neuronal kinesin heavy chain motor protein, was significantly decreased. These data indicate that analyzing the dynamic axon transportome after optic nerve injury identifies acute changes in several protein synthesis and transport homeostatic mechanisms after axon injury.

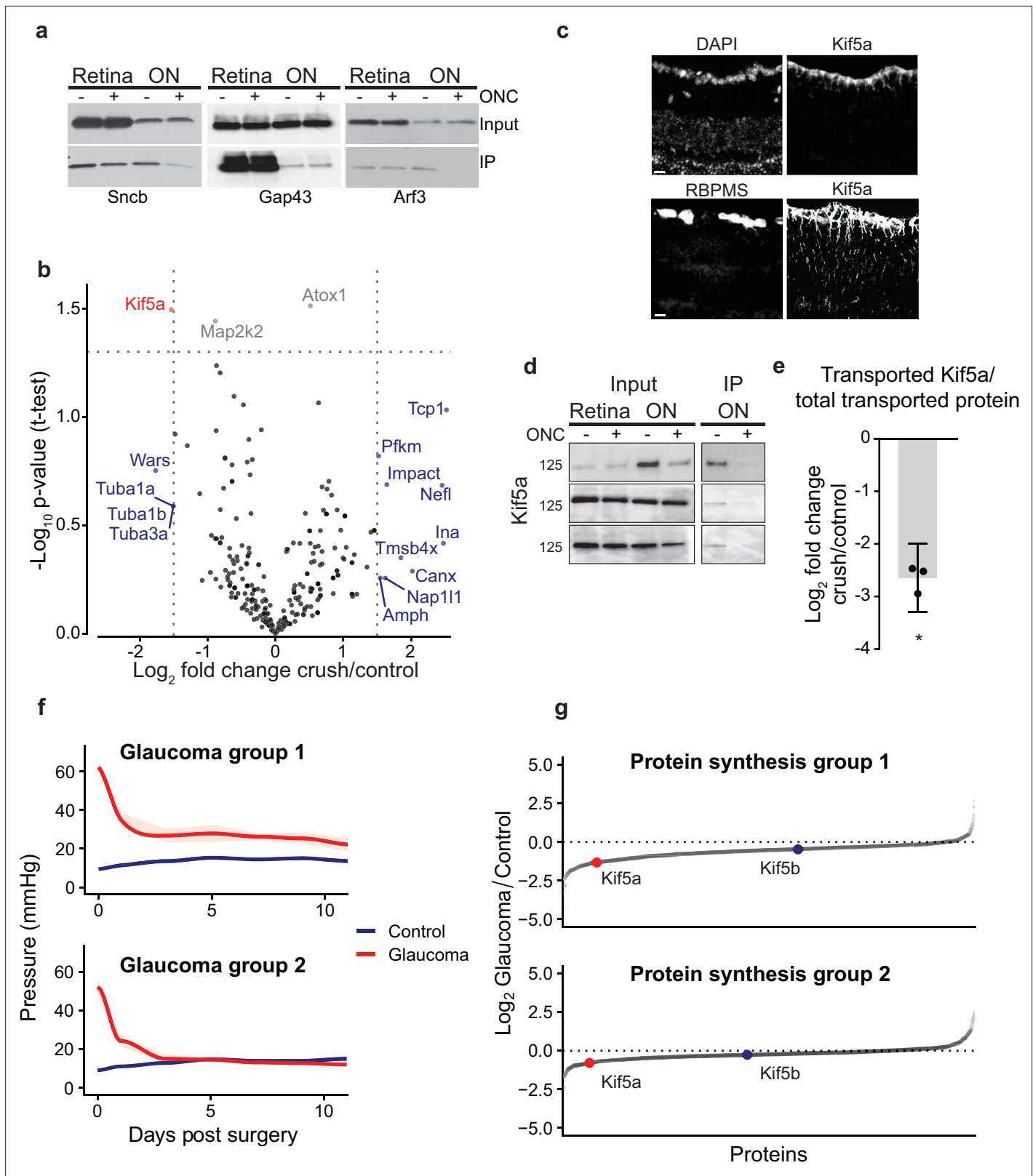


**Figure 2.** Quantitative analysis of proteomics after injury identifies downregulation of Kif5a synthesis and transport after injury. (a) Immunoprecipitation (IP) of biotinylated protein from retinal and optic nerve samples, probed for Snbc, Gap43, or Arf3. Input of each sample on top row, subsequent IP of each sample on bottom row, for either optic nerve crush (ONC) samples or sham surgeries. (b) Volcano plot comparing biotinylated proteins from control versus ONC nerve samples. Normalized spectral abundance factor (NSAF) values for each sample type were averaged across three replicates.

Figure 2 continued on next page

## Figure 2 continued

Proteins with an absolute fold change greater than 1.5, p-value less than 0.05, or both, are colored blue, gray, and red respectively. (c) Retinal cross-sections immunostained with Kif5a and DAPI showing localization of Kif5a in the retinal ganglion cell (RGC) layer (top) and RGC-specific marker RBPM5 and Kif5a showing co-localization of Kif5a with RGCs (bottom). Scale bar, 100  $\mu\text{m}$ . (d) Three replicates of biotin IPs probed with an antibody against Kif5a. Inputs are on the left. The IP was stripped and re-probed for biotin for a measurement of total biotinylated protein pulled down (not shown). (e) Quantification of the change in transported Kif5a compared to the change in total transported protein after ONC. One-sample, two-tailed t-test,  $p = 0.003$ ,  $n = 3$ . The bar height and error bar represent the mean and 95% confidence interval respectively. ONC = optic nerve crush. (f) Average intraocular pressure after induction of glaucoma over time in two groups, one with sustained pressure elevation and one with only initial pressure elevation. (g) Quantitative changes in retinal protein synthesis 3 weeks after induction of glaucoma. 1143 and 1457 proteins were quantified in replicates 1 and 2, respectively.  $\text{Log}_2$  transformed normalized spectral ratios of glaucoma/control samples were plotted from lowest to highest. Newly synthesized Kif5a, detected by BONCAT and quantitative mass spectrometry, was decreased in both replicates, while Kif5b synthesis was unaffected.

The online version of this article includes the following source data and figure supplement(s) for figure 2:

**Source data 1.** Raw western blots for **Figure 2**.

**Figure supplement 1.** Motor protein transport changes after injury and synthesis changes after glaucoma.

**Figure supplement 1—source data 1.** Proteomic quantification of changes in newly synthesized proteins 3 weeks after glaucoma from **Figure 2—figure supplement 1b**.

We confirmed Kif5a expression is localized to RGCs in the mouse retina using immunohistochemistry (**Figure 2c**). We validated the mass spectrometry identification of Kif5a's reduced axon transport by biotin IP and quantitative western blot (**Figure 2d**). We normalized biotin-tagged Kif5a to each sample's total biotin-tagged protein (similar to that shown in **Figure 1f**), and compared injury versus control, which resulted in a significant decrease (about 2.5-fold) in Kif5a transport relative to the decrease in total axon transport after injury (**Figure 2e**), similar to the relative decrease detected by mass spectrometry. Importantly, we saw an equal amount of Kif5a in the retina with and without injury, suggesting that the cause of decreased axon transport is not due to changes in Kif5a abundance in the retina, but in fact reflects a specific anterograde transport deficit. Thus, both western blotting and biotinylated peptide-based mass spectrometry of the axon transportome corroborate Kif5a's reduced axon transport after optic nerve injury.

Kif5a, the only protein that met both significance and magnitude of change criteria, is a motor protein in the 45-member kinesin superfamily (**Hirokawa et al., 2009**). Kinesin-1 motors are composed of two heavy chain and two light chain proteins, where the heavy chains are any of Kif5a, Kif5b, and Kif5c. Of these, Kif5a and Kif5c are neuron-specific, and previously described to be expressed in RGCs (**Rahman et al., 1999; Butowt and von Bartheld, 2007**). When all motor proteins in our transportome data were examined (**Figure 2—figure supplement 1a**), two findings stood out. First, another kinesin heavy chain, Kif5b, did not change in relative transport after injury, suggesting specificity in kinesin isoform transport failure. Second, transport of Klc1, a light chain partner of the heavy chain Kif5a, also was not reduced to the same extent as Kif5a. As kinesin and dynein work in tandem to regulate cargo transport (**Hendricks et al., 2010**), we examined whether there may be similar changes to dynein subunits. We did not discover any significant change in transport of both dynein subunits identified in our transportome, although more work may be needed to explore this question.

### Synthesis of Kif5a, but not Kif5b, is decreased in glaucomatous injury

We also explored changes in Kif5a synthesis after axon injury expanding our investigation to another optic neuropathy, the circumlimbal suture model of glaucoma (**Liu et al., 2015**). Glaucoma is the leading cause of irreversible blindness worldwide and is similarly due to the dysfunction and death of RGCs and their axons. We used the noncanonical amino acid azidohomoalanine (AHA), which is incorporated into newly synthesized proteins in place of endogenous methionine during protein translation (**Schiapparelli et al., 2014; McClatchy et al., 2015**), to selectively quantify newly synthesized proteins over the same 24 hr time period as used in the previous experiments. Three weeks after induction of glaucoma (**Figure 2f**), AHA was injected twice in a 24 hr period as in the experiments described above. After tissue collection, AHA was tagged with biotin using click chemistry, and changes in newly synthesized proteins were quantified with MS/MS. In the retina, 43 proteins showed significant increased synthesis rates and 30 proteins showed significant decreased synthesis rates at this time point in glaucomatous optic neuropathy, normalized to controls. Among these, Kif5a showed decreased synthesis when normalized to the total newly synthesized proteome after induction of

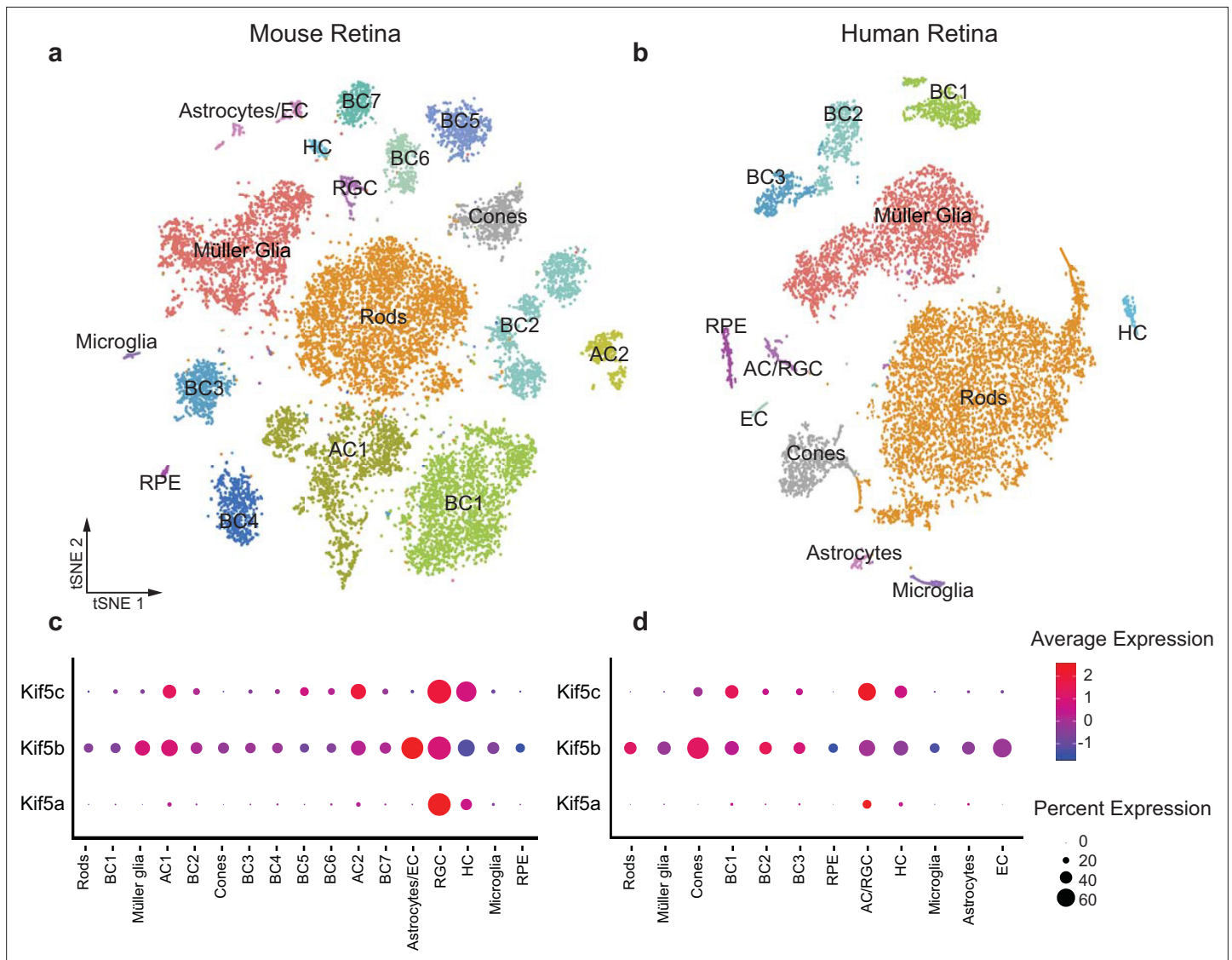


**Figure 3.** *Kif5* expression pattern in the retina is conserved from rodents to humans. (a,b) TSNE plot of cell clustering of single-cell RNA sequencing (scRNA-seq) from either an adult mouse retina or an adult human retina. Clusters defined by canonical cell-specific markers. (c,d) Expression of *Kif5* genes across retinal cell types in either mouse or human retina. *Kif5a* shows highest levels of enrichment in the putative retinal ganglion cell (RGC) clusters in both species, followed by *Kif5c* enrichment. *Kif5b*, conversely, is more ubiquitous across the retina in both species, displaying both conservation of expression patterning across species and divergence of patterning among *Kif5* family members. EC = endothelial cells, BC = bipolar cells, AC = amacrine cells, HC = horizontal cells, RPE = retinal pigment epithelium. Human scRNA-seq data available at GEO: GSE138002 and mouse scRNA-seq data available at GEO: GSE135406.

glaucoma, while *Kif5b* was relatively unchanged (Figure 2g, Figure 2—figure supplement 1b, complete data in ). Together with the acute optic nerve trauma model, these data demonstrate the specificity of changes in synthesis and transport of *Kif5a*, as compared to other *Kif5* isoforms, in both acute and chronic models of optic nerve disease.

### **Kif5 expression in human RGCs**

Given the specificity of *Kif5a* transport failure into RGC axons after optic nerve injury, we wished to explore the expression of *Kif5* mRNA isoforms in RGCs and other retinal cell types. We used single-cell RNA sequencing (scRNA-seq) data from both adult mouse and adult human retinas to determine retinal distribution of kinesin motors and conservation of patterning across species (Getter et al., 2019). We were able to cluster retinal cells into constituent cell types, including a putative RGC cluster (Figure 3a–b). We found that *Kif5a* was enriched in the amacrine cell/RGC cluster of cells compared

to other retinal cell types in both mouse and human, whereas *Kif5b* was expressed more ubiquitously across retinal cell types (**Figure 3c–d**). The conservation of this RGC-enriched expression pattern for both mouse and human retinas further supports a model of kinesin specificity and function.

## Transportomics of Kif5a knockout in RGCs

Given our finding of an association of early Kif5a transport decrease with optic nerve injury, we sought to understand the importance of Kif5a, and its associated cargoes, in RGC function. Discovering specific kinesin-dependent cargoes, for example, by mass spectrometry has not been undertaken, so we hypothesized that characterizing the optic nerve transportome with and without Kif5a should yield Kif5a-dependent cargo localization. For this approach, we used homozygous conditional floxed *Kif5a* adult mice (**Figure 4—figure supplement 1**) as Kif5a knockout mice have seizures and die soon after birth (*Xia et al., 2003; Nakajima et al., 2012*). We delivered either cre-recombinase- or GFP-expressing adeno-associated virus (AAV) intravitreally to specifically knock out Kif5a in adult RGCs. One month after injection, there was almost a complete loss of Kif5a in the retina, and a complete loss in the optic nerve, with neither loss nor compensatory upregulation of Kif5c (**Figure 4a**). We confirmed this loss by immunofluorescence for Kif5a at 1 and 4 months after cre-mediated knockout (**Figure 4b**).

We next explored the Kif5a-dependent transportome. As cre-recombinase requires additional time for expression, recombinase activity, and degradation of existing Kif5a protein, we used a longer time course (3 weeks) to identify the steady-state changes in transport due to Kif5a loss (*Ahmed et al., 2004*). In uninjured mice 3 weeks after intravitreal viral cre injection, we injected NHS-biotin intravitreally three times, each 24 hr apart, to assess changes in the axon transportome using MS/MS as above. This approach identified several proteins with decreased optic nerve axon transport after loss of Kif5a (**Figure 4c**), a number of which are implicated in neuronal injury response and neurodegeneration (complete data in **Figure 4—source data 1**). Bin1, for example, was identified as an Alzheimer's disease locus through GWAS studies (*Seshadri et al., 2010*), and localizes to the axon initial segment and nodes of Ranvier acting downstream of c-myc, an injury-response transcription factor in RGCs (*Belin et al., 2015*). Sh3gl2, also known as endophilin A1, is enriched in synaptic terminals and interacts with synaptic proteins such as synaptojanin and regulates clathrin-mediated synaptic endocytosis (*Milosevic et al., 2011*). We asked whether the proteins whose transport depends on Kif5a expression interact with each other using STRING and were able to group many of these together into three protein-protein interaction networks (**Figure 4d**). Kif5a has already been directly tied to a few of these proteins (*Ishida et al., 2015*), and the presence of potential complexes of non-transported proteins many represent as yet undiscovered functions of Kif5a. Thus these data identify a network of proteins whose transport depends on Kif5a in RGC axons as well as more broadly establish an approach to identify the transportome of motor proteins in vivo.

## Kif5a transport disruption affects anterograde mitochondrial transport in RGCs

We next compared the changes in protein transport seen in optic nerve crush versus Kif5a knockout. We do not expect these entire datasets to correlate given the difference in injury, time course, and model organism, and indeed they do not. However, when we specifically asked how deficits in protein transport after optic nerve crush compared to deficits in protein transport after Kif5a knockout, we find a group of proteins that fulfill both parameters. We focused on protein transport that decreased in both conditions as we hypothesize transport failure contributes to neurodegeneration in both conditions (complete data in **Figure 5—source data 1**). Using Gene Ontology to cluster all proteins that decrease in transport in both optic nerve crush and Kif5a knockout, we discovered a significantly over-represented number of mitochondrial-associated genes in common (**Figure 5a–b**). With this finding, we hypothesized that in both Kif5a transport failure after optic nerve crush and in Kif5a knockout that mitochondrial transport may be specifically downregulated. We tested this hypothesis in primary cultures of RGCs and measured the effect on mitochondrial transport through live cell imaging. AAV2-mediated Kif5a knockdown significantly reduced the average velocity of non-stationary mitochondria compared to an AAV2 scrambled shRNA virus, as shown in kymographs of mitochondrial transport (**Figure 5c–d**). By quantifying the number of mitochondria transported in each direction, we found a significant reduction in anterograde transport (**Figure 5e**). Together, these findings support a model



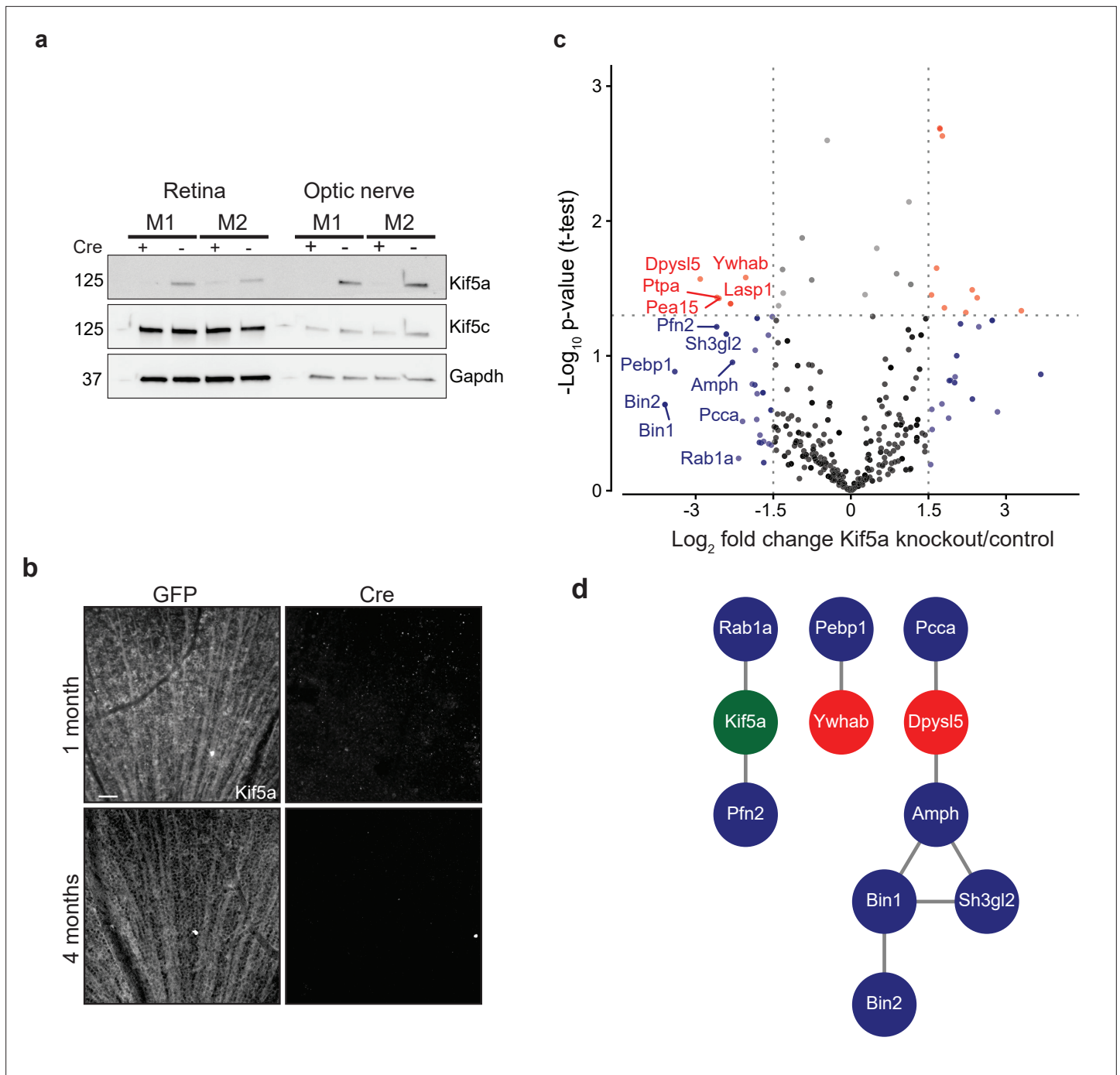


**Figure 4.** Transportomics of Kif5a knockout (KO). **(a)** Western blot validation of Kif5a KO 1 month after intravitreal cre-recombinase injection was apparent in whole retina and optic nerve lysates. Kif5c, a related kinesin, was unaffected by the loss of Kif5a. Cre-positive lanes are designated with a '+', cre-negative lanes are designated with a '-'. Molecular weight on left of blots. **(b)** Wholemount retinas immunostained with an antibody against Kif5a show immunopositive retinal ganglion cell (RGC) axons projecting toward the optic nerve head. Loss of kif5a immunopositive fibers is detected 1 month and is even more pronounced at 4 months after adeno-associated virus (AAV)-cre injection. Scale bar, 50  $\mu$ m. **(c)** Volcano plot comparing biotinylated proteins in the optic nerve 3 weeks after intravitreal AAV-GFP compared to AAV-Cre-GFP. Proteins with a log<sub>2</sub> fold change decrease of greater than 2 after KO are shown in blue, and those which additionally had a p-value less than 0.5 are shown in red. **(d)** STRINGdb interaction diagram for all labeled proteins plus Kif5a create three networks incorporating 11/14 proteins (blue = decrease transport only, red = significantly decreased transport).

The online version of this article includes the following source data and figure supplement(s) for figure 4:

**Source data 1.** Proteomic quantification of transportome changes in Kif5a knockout from **Figure 4c**.

**Source data 2.** Raw western blots for **Figure 4**.

Figure 4 continued on next page

Figure 4 continued

**Figure supplement 1.** Genotype confirmation of conditional Kif5a knockout (KO) mice.

**Figure supplement 1—source data 1.** Raw genotyping blots for **Figure 4—figure supplement 1**.

---

of anterograde mitochondrial trafficking failure in both Kif5a knockout and following optic nerve crush, suggesting a shared biology between injury and loss of Kif5a.

We also tested whether exogenous expression of Kif5a could increase anterograde mitochondrial trafficking. Primary RGCs treated with an AAV2 Kif5a expression virus demonstrated significantly increased average velocity (**Figure 5f–g**). We also found a significant increase in the fraction of anterogradely moving mitochondria compared to control (**Figure 5h**). Thus Kif5a expression is necessary for and can promote anterograde mitochondrial transport in mammalian RGCs.

Kif5a associates with several members of the HnRNP family, including HnRNPA1 (*Kanai et al., 2004*). HnRNPA1 has been shown to play a role in concentration-dependent stress granule formation in other neurodegenerative diseases including ALS (*Kim et al., 2013; Mollieux et al., 2015; Deshaies et al., 2018*). Therefore, we hypothesized that HnRNPA1 knockdown may be deleterious for survival in the context of optic nerve degeneration. We injected a viral vector expressing either an shRNA construct targeting HnRNPA1 or an shRNA scramble construct 2 weeks prior to optic nerve injury and collected retinas 2 weeks after. HnRNPA1 knockdown significantly decreased RGC survival after injury (**Figure 5i–j**). Together, these data further demonstrate the importance of Kif5a and its cargoes in regulation of RGC survival after neurodegenerative injury.

## Kif5a knockout leads to progressive and dose-dependent RGC degeneration

As Kif5a knockout disrupts protein and perhaps mitochondrial transport in the optic nerve, we tested whether the loss of Kif5a affected RGC survival in the absence of optic nerve injury. Using either *Kif5a* or *Kif5b* floxed adult mice and intravitreal AAV-cre delivery, we quantified RGC survival using Brn3a, a nuclear RGC-specific marker, in retinal wholemounts (**Figure 6a**). RGC density did not change 1 month after *Kif5b* homozygous knockout (**Figure 6—figure supplement 1**), but we detected a significant 44% decrease in RGC survival 1 month after *Kif5a* homozygous knockout. This Kif5a-dependent RGC death also led to significant optic nerve atrophy, confirming axonal degeneration in addition to RGC death (**Figure 6b**). We assayed gene dose dependency using a heterozygous *Kif5a*<sup>f/+</sup> mouse line with AAV-cre and found a significant decrease of 22% RGC survival, about half of the cell death seen in the homozygous *Kif5a* knockout (**Figure 6c; 1–2**). To determine if only 44% of RGCs are susceptible to cell death or if Kif5a loss results in progressive degeneration, we aged a cohort of mice to 4 months after knockout and observed an almost complete loss of RGCs (**Figure 6c; 3–4**). To test whether this effect could be a downregulation of Brn3a, we also measured pattern electroretinograms for function of RGCs. Visual responses were almost completely lost 6 months after knockout, quantified by P50 to N95 amplitude (**Figure 6d**). These data indicate that the loss of a specific motor protein Kif5a, but not Kif5b, induces a progressive neurodegeneration as well as a dose-dependent neurodegeneration of RGCs.

We next asked how overexpression of Kif5a would affect RGCs after injury. After validating that our overexpression construct could transport down the optic nerve and bind TUBB3 (**Figure 7a**), we measured the effects on RGC survival. Interestingly, while there were no changes in cell death 1 month post viral injection without injury (**Figure 7b**), there was a 33% decrease in RGC survival after optic nerve crush with Kif5a overexpression compared to control (**Figure 7c–d**). Therefore, maintaining physiological levels of Kif5a transport—and not above or below this level—is crucial for RGC survival after injury.

## Discussion

In diseases such as ALS and glaucoma, axon transport failure has long been proposed to contribute to the pathophysiology of neuronal cell death (*Anderson and Hendrickson, 1974; Minckler et al., 1977; Quigley and Anderson, 1977*). To increase our understanding of the degenerative process, here we quantify the axon transportome separated from surrounding optic nerve glial and other

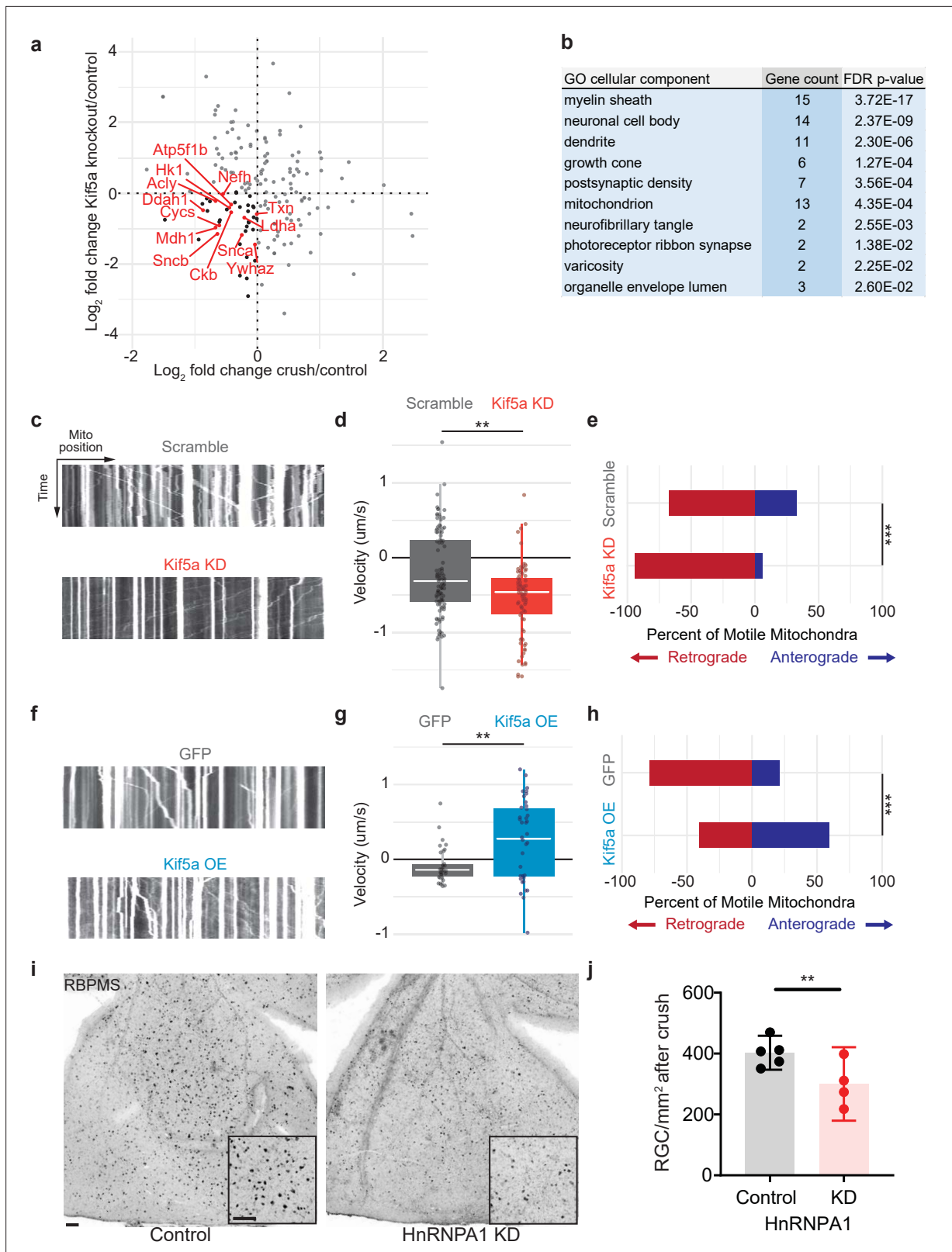


**Figure 5.** Mitochondrial transport is regulated by Kif5a in retinal ganglion cells (RGCs). **(a)** Log<sub>2</sub> comparison of protein transport changes in Kif5a knockout (KO) compared to optic nerve crush. Proteins in the lower left quadrant are decreased in both conditions. Proteins in red are identified as associated with Gene Ontology (GO) cellular component ‘mitochondrion’. Proteins in black are non-mitochondrial. **(b)** Top GO cellular component ontologies for over-representation with shared hierarchy terms removed. ‘Gene count’ refers to number of genes in bottom left quadrant (decreased in

Figure 5 continued on next page

## Figure 5 continued

transport after Kif5a KO and optic nerve crush [ONC] out of total genes in common between the two datasets. Full enrichment list found in **Figure 5—source data 2**. **(c,f)** Representative kymographs of mitochondrial movement in isolated E18 RGC neurites using MitoTracker deep red after viral delivery of either Kif5a shRNA or scramble shRNA **(c)** or Kif5a overexpression or GFP **(f)**. Images captured by time-lapse confocal microscopy. **(d,g)** Quantification of average mitochondrial velocity. Each data point represents a single mitochondrion. Boxplot covers the interquartile range with median noted in white. Two-sample, two-tailed t-test,  $p < 0.0001$  (cultures = 3; Kif5a KD mito = 100; neurons = 19, scramble mito = 117; neurons = 18),  $p = 0.002$  (cultures = 3; Kif5a OE mito = 52; neurons = 13, GFP = 42; neurons = 22). **(e,h)** Proportion of retrogradely moving mitochondria versus anterogradely moving mitochondria. Fisher's exact test,  $p < 0.0001$  (top),  $p = 0.0003$  (bottom). **(i)** Representative example of wholemount retinas 2 weeks after ONC stained with RGC-specific marker RBPMS, after either intravitreal adeno-associated virus (AAV)-scramble-shRNA or AAV-HnRNPA1-shRNA injection. For both wholemount and inset: scale bar, 100  $\mu\text{m}$ . **(j)** Quantification of RBPMS + cell density after ONC across entire retinal surface. Each point represents one retina (control  $n = 5$ , KD  $n = 4$ ). Two-sample, two-tailed t-tests,  $p = 0.039$ .

The online version of this article includes the following source data for figure 5:

**Source data 1.** Protein-by-protein comparison of fold change in ONC compared to Kif5a knockout from **Figure 5a**.

**Source data 2.** Cellular component Gene Ontology using the PANTHER platform for **Figure 5b**.

cells' proteomes, and for the first time describe specific changes in the complement of transported proteins after injury. Previous approaches to characterizing axon-specific protein responses to injury depended on physically extracting cytoplasm from axons in whole nerve preparations (*Michaielevski et al., 2010*), a technically challenging approach with inconsistent results noted by those authors. We previously established an in vivo protein biotinylation, mass spectrometry-based axon transportome approach which requires amine reactivity to study steady-state protein transport in the visual system. While this labeling method requires available amine-groups, previous work characterizing the types of proteins identified by NHS-biotin did not show any particular bias compared to unlabeled proteomics (*Schiapparelli et al., 2014; Schiapparelli et al., 2019*). Here, adapting this technique to NHS-biotin injections within a 24 hr window allowed us to capture spatial and temporal dynamics in axonal protein transport immediately following axon injury and contribute three major new findings.

First, this improved temporal resolution quantitatively detected loss of specific proteins' transport before total protein changes are apparent, as seen comparing western blotting of whole tissue to IP of biotinylated proteins. In fact, many of the axonal changes that occur after injury may begin earlier than previously thought, with rapid changes to the axon transportome. Additional examination of the time course of axon transport changes in the period after injury or in other models of neurodegenerative diseases may now be addressed through such time-resolved quantitative proteomics in future studies. The tradeoff from increasing temporal resolution and dissecting the fraction of transported proteins from the surrounding milieu is a decrease in the total number of identified, labeled peptides available for quantification. Current, state-of-the-art mass spectrometers allowed discovery of some of the transportome changes, but not of transported proteins below the detection threshold. Future advances in proteomics will allow for deeper sequencing and likely to identification of additional biologically relevant transportomic changes.

Second, using this novel approach for quantifying axonal protein transport, we identify a specific transport failure of Kif5a in RGC axons early in the degenerative course following optic nerve injury. Disruptions to the kinesin motor protein family manifest in a variety of neurological diseases. Charcot-Marie-Tooth disease type 2A can be caused by mutations in Kif1b (*Zhao et al., 2001*), congenital fibrosis of the extraocular muscles can be caused by mutations in Kif21a, and a loss-of-function mutation in Kif5a motor domain can result in hereditary spastic paraplegia (*Reid et al., 2002; Xia et al., 2003; Tessa et al., 2008; Morfini et al., 2009*). Different loss-of-function mutations in Kif5a, all affecting the cargo binding domain, are causative in some cases of ALS (*Brenner et al., 2018; Nicolas et al., 2018*). In this study, we identified both acute transport failure of Kif5a, without a concomitant change in retinal abundance, after acute optic nerve injury and a decrease in new protein synthesis of Kif5a 3 weeks after initiation of a chronic glaucoma model. These orthogonal experiments using separate protein labeling paradigms both point toward downregulation of Kif5a as part of an overall maladaptive response of RGCs to injury.

Third, these data open a new direction for study of transport biology, to better understand motor protein cargo specificity and physiology. The finding of Kif5a transport failure after injury is especially interesting given the relative lack of change in other motor proteins, such as Kif5b. Increasing evidence has shown that kinesin subtypes and adaptor proteins have at least partial cargo specificity

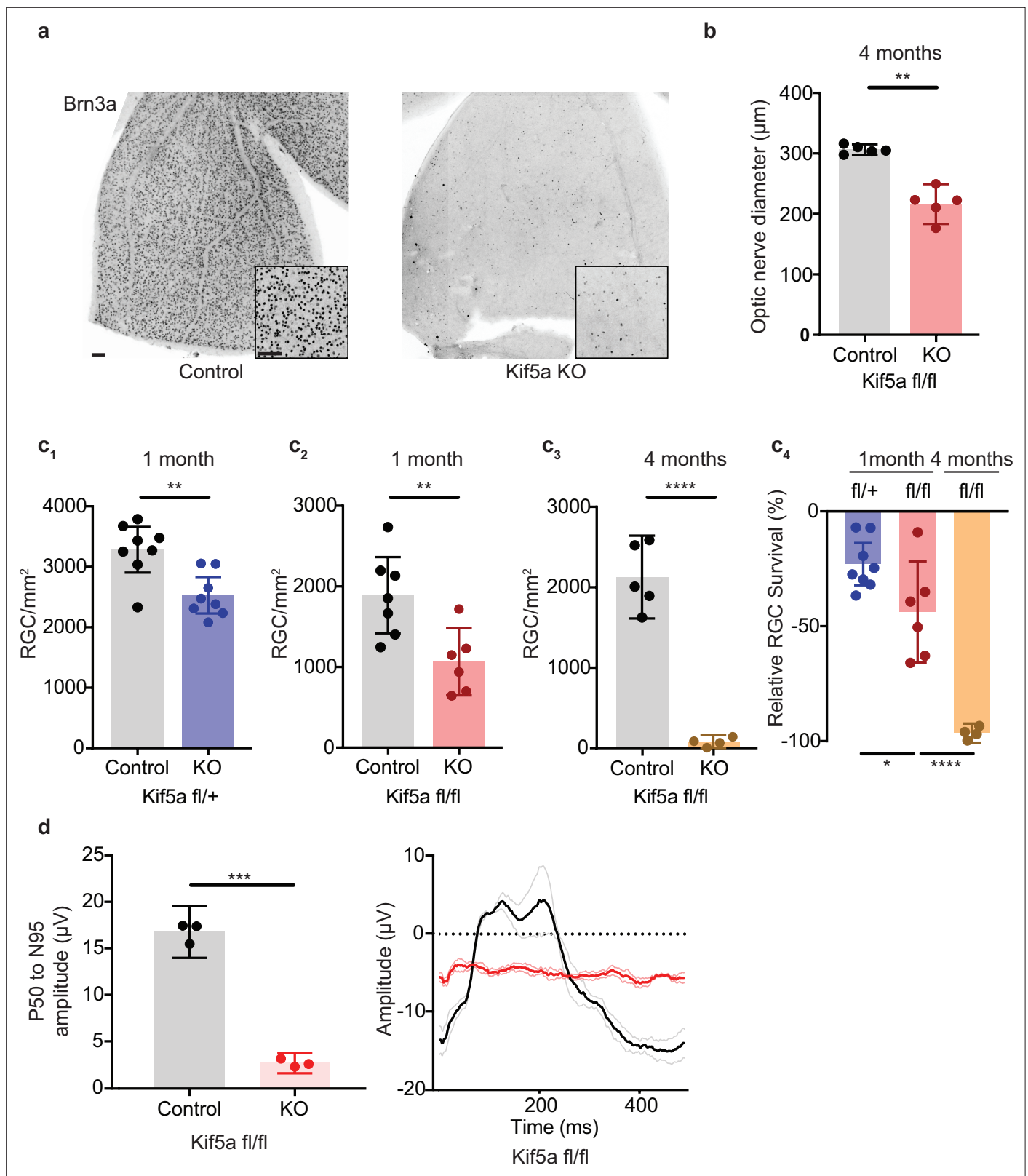


**Figure 6.** Kif5a knockout (KO) leads to progressive, dose-dependent retinal ganglion cell (RGC) degeneration. **(a)** Representative example of wholemount Kif5a<sup>fl/fl</sup> retinas stained with RGC-specific marker Brn3a, 4 months after either intravitreal adeno-associated virus (AAV)-GFP or AAV-Cre-GFP. Scale bar = 100  $\mu\text{m}$  for both wholemount images and insets. **(b)** Quantification of the average diameter of optic nerve cross-section taken halfway between the optic nerve chiasm and optic nerve head in either control or Kif5a knockout (KO) animals (control n = 5, KO n = 5). Two-sample, two-tailed

Figure 6 continued on next page

Figure 6 continued

t-test,  $p = 0.001$ . (c) Quantification of Brn3a + cell density across entire wholemount retinal surface. Each point represents one retina. The graphs, from left to right, show pairwise comparisons between heterozygous Kif5a KO at 1 month after viral injection (control  $n = 8$ , KO  $n = 8$ ), homozygous Kif5a KO at 1 month after viral injection (control  $n = 7$ , KO  $n = 6$ ), homozygous Kif5a KO at 4 months after viral injection (control  $n = 5$ , KO  $n = 4$ ), and a comparison of the three previous experiments normalized to their control population.  $C_1$ - $C_3$  are two-sample, two-tailed t-tests,  $p = 0.003$ ,  $p = 0.008$ , and  $p < 0.0001$ , respectively.  $C_4$  is a one-way ANOVA with post hoc Sidak correction. Between the blue and red columns,  $p = 0.034$ . Between red and gold columns,  $p < 0.0001$ . The bar heights represent the mean, and the error bars represent the 95% confidence interval. (d) Pattern electroretinogram quantification from mice 6 months after Kif5a KO or control. On the left, the amplitude difference between the P50 peak and the N95 trough was quantified and compared with a two-sample, two-sided t-test ( $n = 3$ ),  $p < 0.0001$ . The bar heights represent the mean, and the error bars represent the 95% confidence interval. On the right, the average traces of each condition are bold, with lighter shades  $\pm$  SEM.

The online version of this article includes the following figure supplement(s) for figure 6:

**Figure supplement 1.** Loss of Kif5b does not lead to RGC cell death.

(Chevalier-Larsen and Holzbaaur, 2006), yet the extent of shared and specific cargo between kinesin proteins is not fully understood. Through IP and immunoprecipitation assays, several synaptic proteins such as Snap25, synaptotagmin, and syntaxin 1a have been identified as cargoes of the Kif5 family (Toda et al., 2008), but only a few proteins have been shown to be specific to Kif5a, such as GABARAP (Nakajima et al., 2012). Quantitative changes in cargo transport after the loss of a specific motor protein may give insight into the role of that motor, and future studies could expand on these data by directly comparing the axon transportome of different kinesin isoforms.

Specificity of function between these closely related motor proteins was also an important finding in these data. Kif5a loss, but not Kif5b loss, resulted in the progressive, dose-dependent degeneration of adult RGCs; this specificity mirrored the specificity of Kif5a's decreased axon transport detected after optic nerve injury, and the enrichment of Kif5a in mouse and human RGCs contrasted with the ubiquitous expression of Kif5b. Although overexpression of Kif5a did not increase RGC survival after injury, the conservation of RGC-enriched Kif5a expression across species suggests a strategy of manipulating Kif5a therapeutically to restore axonal transport after injury or in neurodegenerative diseases like glaucoma. This approach, along with further characterization of Kif5 expression in RGC subtypes, would be intriguing next steps in understanding motor protein biology.

Although here we describe initial data on the axon transportome cargoes dependent on Kif5a for their RGC axon localization, we do not yet understand which cargoes of Kif5a contribute to optic neuropathy, especially in vivo. By quantifying the transportomic changes in an adult acute knockout model, it is possible that we identified only the subset of proteins whose transport was not adequately compensated by other mechanisms or motors. Indeed, bioinformatic analysis indicates that many of these protein cargoes have known interactions with each other, and several have previously been reported as associated with degenerative diseases in other systems. Another possibility is that these proteins, instead of being direct cargoes of Kif5a, are downregulated or mis-localized after Kif5a loss. Increased protein degradation would also contribute to decreased detection of biotinylated proteins, as detection of transported proteins is the net of protein transport and protein degradation. Finally, these data are limited to transported proteins. Kif5a can act as a motor for fast axonal transport of membranous organelles, slow axonal transport of proteins, and transport of neurofilaments (Xia et al., 2003). In addition, cargoes can include mRNA and related P-bodies and stress granules for local protein synthesis (Loschi et al., 2009; Oh et al., 2013). Our finding that knockdown of one such ribonucleoprotein cargo of Kif5a, HnRNPA1, results in exacerbated degeneration after injury suggests that the loss of Kif5a-dependent RNA and other organelle transport may also contribute to neurodegeneration. In particular, stress granules have been implicated in at least one form of glaucoma (Lachke et al., 2011), which combined with our data suggests exploring the role of both stress granules and mitochondria as disease-relevant Kif5a cargo as an exciting future direction.

Indeed, the over-representation of mitochondrial-associated proteins demonstrating decreased axon transport in both of our datasets point toward a lack of mitochondrial transport after loss of Kif5a. The short time point assayed in our optic nerve injury model (24 hr) is consistent with the rapid halt of mitochondrial transport in RGC axon in an ocular hypertension/glaucoma model (Takahara et al., 2015). Kif5 motors regulate mitochondrial trafficking in *Drosophila* and mammalian hippocampal neurons through the adaptor proteins Milton and Miro (Glater et al., 2006; Macaskill et al., 2009). Mitochondrial localization in axons regulates both neuronal survival and axon regeneration. In

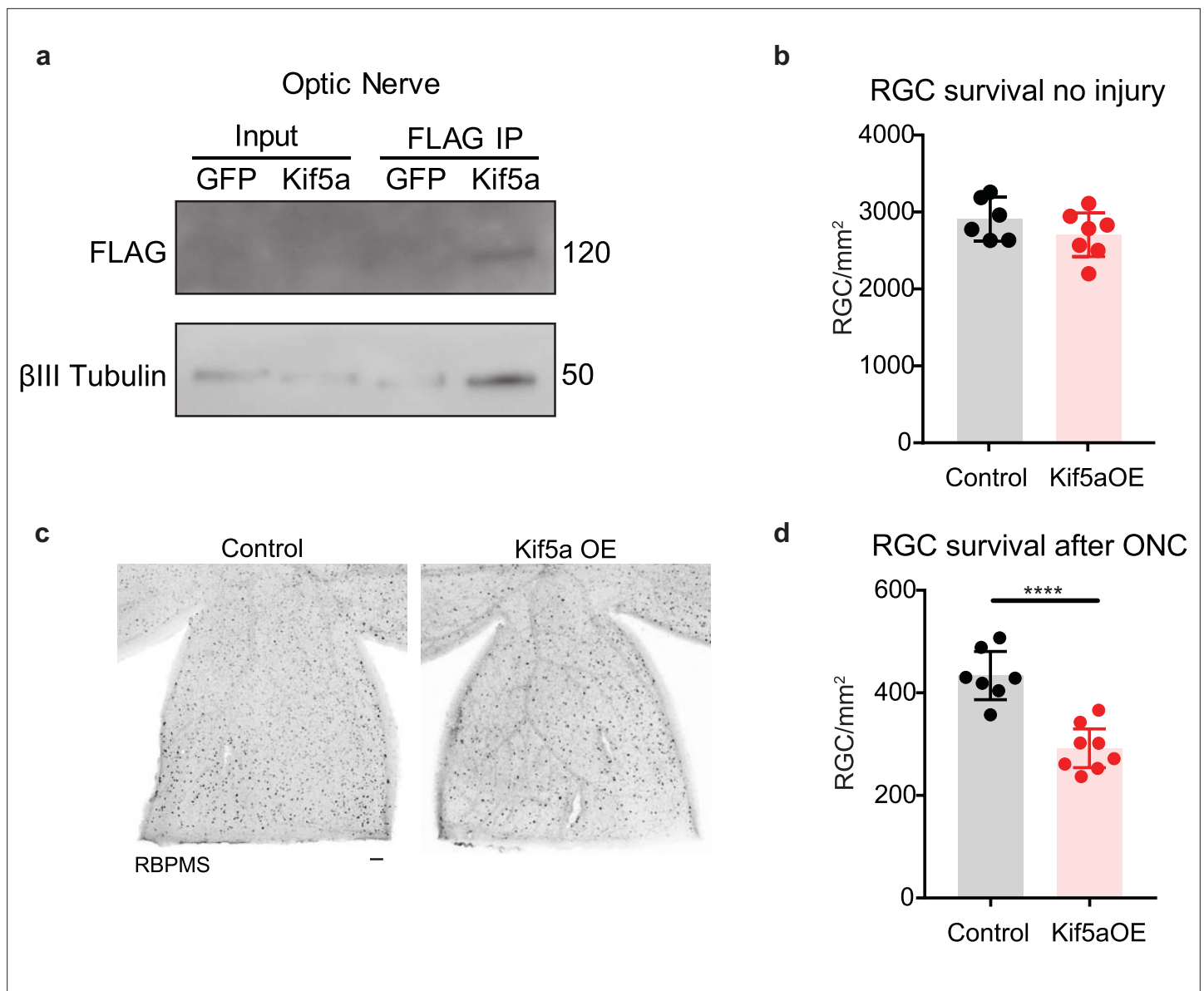


**Figure 7.** Kif5a overexpression exacerbates retinal ganglion cell (RGC) death. **(a)** Optic nerves were collected 2 weeks after intravitreal injection of adeno-associated virus (AAV)-Kif5a-FLAG. Immunoprecipitation showed the presence of FLAG-tagged protein at the molecular weight of Kif5a. Co-immunoprecipitation of  $\beta$ -III tubulin confirmed that overexpressed Kif5a transported to the optic nerve and bound to the cytoskeleton. **(b)** RGC survival was not affected 4 weeks after viral injection of Kif5a compared to a control GFP virus (control  $n = 6$ , OE  $n = 7$ ). Two-tailed, two-sample, t-test. **(c)** Representative example of wholemount retinas stained with RBPMS, an RGC-specific marker, 2 weeks after optic nerve crush, injected with either AAV-GFP or AAV-Kif5a-FLAG 2 weeks before crush. Scale bar, 100  $\mu$ m. **(d)** Quantification of RBPMS + cell density after optic nerve crush (ONC) across entire retinal surface. Each point represents one retina (control  $n = 7$ , OE  $n = 8$ ). Two-sample, two-tailed t-tests,  $p < 0.0001$ .

The online version of this article includes the following source data for figure 7:

**Source data 1.** Raw western blots for **Figure 7**.

*Caenorhabditis elegans*, mitochondria localize to injured axons during the normal course of regeneration (Han et al., 2016). In non-regenerating neurons, like mammalian RGCs, manipulating mitochondrial mobilization through overexpression of Armcx1 produces a similar survival and regenerative effect (Cartoni et al., 2016). Previous studies have shown that Kif5a may regulate mitochondrial transport in zebrafish (Campbell et al., 2014) and cultured hippocampal neurons (Chen and Sheng, 2013). However, it was not known if Kif5 motors regulate mitochondrial trafficking in RGC neurons in vitro or in vivo or if manipulating Kif5a alone is sufficient to affect mitochondrial transport, both hypotheses

now supported with these new data. Combining these two findings, we hypothesize that targeted anterograde transport of mitochondria to the injured mammalian axon could potentially enhance the effects already seen with *Armcx1*-mediated mitochondrial mobilization. Overexpression of Kif5a in RGCs in vitro preferentially increases anterograde mitochondrial transport, increasing mitochondrial concentration in the axon, raising the question of whether overexpressing Kif5a in vivo would promote RGC survival. Interestingly, overexpression of Kif5a led to increased cell death after injury. However, Kif5a abundance in the retina is unchanged after optic nerve injury, suggesting that loss of optic nerve localization is specific to axon transport failure rather than to deficit of Kif5a expression itself. Regulation of kinesin transport is known to depend on phosphorylation states (*Morfino et al., 2001*), calcium-dependent inhibition by mitochondrial cargo (*Wang and Schwarz, 2009*), conformational state changes by kinesin light chains, inhibition by MAP2 at the axon initial segment (*Gumy et al., 2017*), and autoinhibition of the motor domain by inactive kinesin heavy chains (*Cai et al., 2007*). Removing autoinhibitory domains or truncation of the motor beyond the first coiled-coil domain creates constitutively active kinesins, potentially circumventing any inherent axonal inhibition (*Yang et al., 2016*). Future work specifically restoring anterograde protein and mitochondrial trafficking in the face of axonal injury, perhaps using constitutively active Kif5a mutants, could rescue cell death and provide therapeutic avenues to counter the neurodegenerative process.

## Materials and methods

### Key resources table

Reagent type (species) or resource	Designation	Source or reference	Identifiers	Additional information
Strain, strain background ( <i>Mus musculus</i> )	Wild-type	The Jackson Laboratory	C57BL/6	Pooled sexes
Strain, strain background ( <i>Mus musculus</i> )	Kif5a <sup>fl/fl</sup>	David Williams Laboratory	MMRRC:MMRRC_000224-UCD	Pooled sexes
Strain, strain background ( <i>Mus musculus</i> )	Kif5b <sup>fl/fl</sup>	David Williams Laboratory	JAX stock:008637	Pooled sexes
Strain, strain background ( <i>Rattus norvegicus</i> )	Wild-type	The Jackson Laboratory	Sprague-Dawley	Pooled sexes
Cell line (Human)	HEK 293T	ATCC	293T	
Other	Viral Vector AAV2-GFP	UPenn Vector Core	AV-2-PV0101	
Other	Viral Vector AAV2-cre-GFP	UPenn Vector Core	AV-2-PV2004	
Other	Viral Vector AAV2-Kif5a	This paper	VectorBuilder ID: <a href="https://en.vectorbuilder.com/vector/VB170708-1017enf.html">https://en.vectorbuilder.com/vector/VB170708-1017enf.html</a>	Sui Wang Laboratory; Vector Map from VectorBuilder
Other	Viral Vector AAV2-Kif5a shRNA	This paper	VectorBuilder ID: <a href="https://en.vectorbuilder.com/vector/VB180108-1217eru.html">https://en.vectorbuilder.com/vector/VB180108-1217eru.html</a>	Sui Wang Laboratory; Vector Map from VectorBuilder
Antibody	Rabbit anti-Kif5a	Abcam	Ab5628	(1:1000)
Antibody	Rabbit anti-Kif5c	Abcam	Ab192883	(1:1000)
Antibody	Goat anti-biotin	Thermo	31852	(1:1000)
Antibody	Rabbit anti-FLAG	CST	14793S	(1:2000)
Antibody	Rabbit anti-B3Tubulin	CST	5568S	(1:2000)
Antibody	Rabbit anti-GAPDH	CST	2118	(1:2000)

Continued on next page



Continued

Reagent type (species) or resource	Designation	Source or reference	Identifiers	Additional information
Antibody	Rabbit anti-SNCFB	Sigma	SAB1100305	(1:2000)
Antibody	Rabbit anti-GAP43	Novus	NB300	(1:5000)
Antibody	Rabbit anti-ARF3	Abcam	Ab154383	(1:5000)
Antibody	Goat anti-mouse	Abcam	Ab6789	(1:2000)
Antibody	Goat anti-rabbit	Abcam	Ab6721	(1:2000)
Antibody	Donkey anti-goat	Abcam	Ab97110	(1:2000)
Antibody	Mouse anti-Brn3a	Millipore	MAB1585	(1:100)
Antibody	Rabbit anti-RBPMS	PhosphoSolutions	1830-RBPMS	(1:300)

### Animal lines

C57BL/6 mice or Sprague-Dawley rats of either sex were used for all wild-type experiments. *Kif5a<sup>fl/fl</sup>* and *Kif5b<sup>fl/fl</sup>* from a C57BL/6 background were a gift from David Williams (*Xia et al., 2003*).

### Intravitreal injection

Sprague-Dawley rats or mice (30–45 days of age) were used for all experiments. A microinjector pressure system (Picosprizer II) with a pulled glass micropipette in a micromanipulator was used to inject reagents intravitreally. For viral injections, mice were injected intravitreally with 1.5  $\mu$ l volume of AAV2-GFP or AAV2-cre-GFP (UPenn Vector Core) (titers ranged from 0.5 to  $1 \times 10^{13}$  genome copies/ml). For in vivo biotinylation experiments, 5 mg of NHS-biotin (EZ-Link from Pierce) were dissolved in 300  $\mu$ l of sterile DMSO immediately prior to use, as described previously (*Schiapparelli et al., 2019*). For in vivo AHA experiments, we injected each eye with  $\sim$ 5  $\mu$ l of 400 mM AHA in PBS. Briefly, intravitreal injections (5  $\mu$ l for rats, 1.5  $\mu$ l for mice) were given to both eyes. The injections were given twice over 24 hr under deep anesthesia with either 0.5 mg/kg medetomidine and 75 mg/kg ketamine intraperitoneal, or 2% isoflurane under nose cone. The eyes were treated with topical antibiotics and analgesics.

### Optic nerve crush

Under deep anesthesia, the optic nerve was exposed and crushed using fine forceps (Dumont #5) at 1.5 mm behind the optic nerve head for 5 s. Care was taken to avoid damaging the blood supply to the retina. Sham surgeries exposed the optic nerve, but no crush was given. All optic nerve crush procedures were performed by a surgeon blinded to the viral treatment. Postoperatively, animals were allowed to recover on a heating pad and were given subcutaneous injections of buprenorphine hydrochloride, 0.1 mg/kg, twice a day for 3 consecutive days to minimize discomfort.

### Circumlimbal glaucoma model

Baseline intraocular pressure (IOP) of adult rats was measured using a rebound tonometer (Tonolab; iCare, Helsinki, Finland) under inhaled isoflurane anesthesia. Eyes were randomized to either circumlimbal glaucoma or sham. To induce glaucoma, a circumlimbal suture (7/0, nylon) was tied around the eye 1.5 mm behind the limbus with five anchor points. In the glaucoma group, the suture was tied tightly, with intraoperative IOP measurements greater than 40 mmHg. In sham eyes, the suture was tied loosely. IOP measurements were taken every other day between 2 PM and 6PM under isoflurane anesthesia.

### Pattern electroretinogram

Anesthetized mice were placed on a feedback-controlled heating pad (TCAT-2LV, Physitemp Instruments Inc, Clifton, NJ) to maintain body temperature at 37°C. Simultaneous binocular PERG recording was completed with the Miami PERG system (Intelligent Hearing Systems, Miami, FL) according to published protocol (*Chou et al., 2018*). Eye drops were added as needed to prevent corneal drying

(Systane Ultra Lubricant Eye Drops, Alcon Laboratories, Ft Worth, TX). The reference electrode was placed subcutaneously on the back of the head between the two ears and the ground electrode was placed at the root of the tail. The signal electrode was placed subcutaneously on the snout for the simultaneous acquisition of left and right eye responses. Two 14 cm × 14 cm LED-based screens were placed 10 cm in front of each eye. The pattern remained at a contrast of 85% and a luminance of 800 cd/m<sup>2</sup>, and consisted of four cycles of black-gray elements, with a spatial frequency of 0.052 c/d. Upon stimulation, the PERG signals were recorded by asynchronous binocular acquisition. Two consecutive recordings of 200 traces were averaged to achieve one readout. The first positive peak in the waveform was designated as P50 and the second negative peak as N95. The investigators who measured the amplitudes were blinded to the treatment of the samples.

## Immunohistochemistry

At different time points after surgeries, animals were deeply anesthetized and transcardially perfused with 4% PFA in PBS. Optic nerves and retinas were dissected and fixed in 4% PFA for 1 hr and subsequently washed in PBS. Optic nerves were sequentially incubated in 15% and 30% sucrose at 4°C overnight before mounting in optimal cutting temperature mounting medium for sectioning. Retinas were kept in PBS at 4°C until ready for antibody staining. Retinas were incubated with mouse anti-Brn3a (1:100; Millipore, MAB1585) and rabbit anti-Rbpms (1:300; PhosphoSolutions, 1830-RBPMS), both specific markers of RGCs, and anti-Kif5a (1:300, Abcam ab5628). Secondary antibodies were Alexa Fluor 488-, 594-, or 647-conjugated, highly cross-adsorbed antibodies (1:500; Invitrogen). Wholemount retinal images were acquired using a laser scanning confocal microscope (Carl Zeiss 880 or Olympus FV500) and quantified by a researcher blinded to the experimental condition. Biotinylated optic nerves sections were incubated with 100 mM glycine in PBS for 2 hr and endogenous peroxidase activity was blocked with 0.5% of H<sub>2</sub>O<sub>2</sub> and 1% normal goat serum (NGS) in PBS for ½ hr. Sections were blocked with 10% NGS in PBS for 1 hr and incubated overnight with ABC reagent (1 drop of A and 1 drop of B in 5 ml PBS with 1% NGS, Vector Lab). Signal was amplified using tyramide amplification system (TSA kit, PerkinElmer) conjugated to Alexa Fluor 488.

## RGC quantification

The RBPMS quantification were performed in a masked fashion as previously described (*Wang et al., 2015*). Briefly, the retinas were divided into four quadrants, and one digital micrograph was taken from a fixed distance from the periphery of each of the four fields. Whole retina Brn3a was quantified using a semi-automated protocol in Velocity (PerkinElmer) and ImageJ in a masked fashion. Tiled images of entire retinal wholemounts were imported into ImageJ for quantification of total area. During this step, care was taken to remove sections of retina damaged during tissue processing. These modified images were then moved to Velocity, where 'Find object' using thresholds for minimum object size, intensity, and touching neighbors. Once the protocol was set for one randomly selected retina, it was applied to all retinas in the experiment.

## FUNCAT

NHS-Azide-injected samples were processed for click chemistry according to the following protocol, modified from previous studies (*Dieterich et al., 2010; Hinz et al., 2012*). Sections or wholemounts were transferred to Eppendorf tubes or six-well plates with reaction mixture composed of 100 μm Tris[(1-benzyl-1H-1,2,3-triazol-4-yl)methyl]amine (TBTA, Sigma) dissolved in 4:1 tBuOH/DMSO (Sigma), 100 μm CuSO<sub>4</sub> (Sigma), 1.25 μm Alexa Fluor 488 alkyne (Invitrogen), and 250 μm tris(2-carboxyethyl) phosphine (TCEP, Sigma). The reaction proceeded overnight at room temperature.

## Biotin click reaction

Optic nerves or retinas were lysed in 0.5% SDS in PBS plus a cocktail of endogenous protease inhibitors (Complete Protease Inhibitor Cocktail Tablets, Roche) by homogenizing and sonicating with 10 pulses using a tip sonicator (Sonic Dismembrator model 100, Fisher Scientific). Samples were boiled for 10 min and cooled to room temperature. Any remaining insoluble material was resuspended with additional sonication pulses. Protein concentration in the suspension was measured, and aliquots of 1.5 mg of protein suspension were transferred to eppendorf tubes. NHS-azide or AHA that was incorporated into proteins was labeled with PEG4 carboxamide-Propargyl Biotin (biotin-alkyne) (Invitrogen)

by click chemistry reaction performed in the total protein suspension as described previously (*Speers and Cravatt, 2009; Hulce et al., 2013*). For AHA samples, click reactions were done using biotin-alkyne labeled with heavy stable carbon and nitrogen isotopes: biotin-beta-alanine- $^{13}\text{C}_3$ ,  $^{15}\text{N}$ -alkyne [Biotin Propargyl amide] or light isotope forms of the alkyne (#7,884 and #7889, respectively; Setareh Biotech) in the different experimental groups. Centrifugation steps that can result in loss of NHS azide- or AHA-labeled material were avoided. For each reaction, an aliquot of 1.5 mg of protein suspension was used, adding PBS to reach 346  $\mu\text{l}$  before adding the click reaction reagents. We added the following reagents in sequence, vigorously vortexing after each addition: 30  $\mu\text{l}$  of 1.7 mM TBTA (Sigma) dissolved in 4:1 *tert*-butanol/DMSO (Sigma), 8  $\mu\text{l}$  of 50 mM  $\text{CuSO}_4$  dissolved in ultrapure water (Sigma), 8  $\mu\text{l}$  of 5 mM of PEG4 carboxamide-propargyl biotin (biotin-alkyne) (Invitrogen) dissolved in DMSO, and 8  $\mu\text{l}$  of 50 mM TCEP (Sigma) dissolved in water. The click reactions were incubated at room temperature for 1–2 hr or overnight with gentle rotation at 4°C. After the completion of each click reaction, samples were aliquoted by transferring 200  $\mu\text{l}$  of each click reaction suspension to 2 ml eppendorf tubes.

### Fresh tissue collection

Rats or mice were euthanized with  $\text{CO}_2$  and decapitated for brain removal. The tissue was frozen immediately in isopentane in dry ice and stored at  $-80^\circ\text{C}$  for biochemistry studies. Co-immunoprecipitation studies continued directly without freezing.

### IP and western blot

For western blot, after defrosting frozen tissue the retinas or optic nerves were dissected and homogenized by sonication in 50–100  $\mu\text{l}$  RIPA Lysis Buffer with protease and phosphatase inhibitor cocktail (Holt, 78440). Samples were centrifuged at 10,000 $\times g$  for 10 min at 4°C, and the supernatants collected. Total protein concentration was determined using a BCA assay (Pierce BCA Protein Assay Kit 23225).

To purify biotinylated proteins for western blot validation, 0.8–2 mg of proteins from ON or retinal homogenates in a total volume of 1 ml were incubated with 30  $\mu\text{l}$  neutravidin beads (Thermo) at 4°C overnight. The beads were then washed 6 times with 1 ml of RIPA buffer. The bound biotinylated proteins were eluted from the beads with 50  $\mu\text{l}$  Laemmli sample buffer containing 2.5% of 2-mercaptoethanol.

For co-immunoprecipitation, retinas and optic nerves were mechanically homogenized in buffer (20 mmol/l HEPES, pH 7.4, 150 mmol/l NaCl, 5 mmol/l EDTA, 0.5% Triton, 50 mmol/l NaF, 1 mmol/l sodium orthovanadate, 1 mmol/l DTT, and protease inhibitors). After centrifugation at 10,000 $\times g$  for 10 min at 4°C, the clarified extracts were used for IP using appropriate antibodies (2  $\mu\text{g}$  rabbit anti-FLAG, CST, 14793S) and 20  $\mu\text{l}$  protein G sepharose (Millipore, Fastflow) for 3 hr to at 4°C. The beads were washed 3–5 times with lysis buffer, and the immunoprecipitated proteins were eluted with 2 $\times$  Laemmli buffer for western blotting.

For all electrophoresis, 10–30  $\mu\text{g}$  of protein was loaded on a 4–20% Tris-Glycine Gel (Thermo Fisher Scientific XP04202) and transferred to an activated 0.2  $\mu\text{m}$  PVDF membrane for immunoblotting. The membranes were saturated with Ponceau S stain for 5 min and imaged, before washing with ddH $_2\text{O}$ . The membranes were saturated with TBS 1 $\times$ , 0.05% Tween-20, and 5% nonfat dry milk for 1 hr at room temperature, then incubated overnight at 4°C with rabbit anti-Kif5a (1:1000, Abcam, ab5628), rabbit anti-Kif5c (1:1000, Abcam, ab192883), goat anti-biotin (1:1000, Thermo, 31852), rabbit anti-FLAG (1:2000, CST, 14,793S), rabbit anti- $\beta$ -III tubulin (1:2000, 5568S, CST), rabbit anti-GAPDH (1:2000, CST, 2118), rabbit anti-SNCB (1:1000, Sigma), rabbit anti-GAP43 (1:5000, Novus), rabbit-ARF3 (1:1000, Abcam). All membranes were washed with TBS-Tween between incubations. The membranes were then saturated with peroxidase-conjugated goat anti-mouse, anti-rabbit, or anti-goat (1:2000, Abcam, ab6789, ab6721, and ab97110) secondary antibodies for 3 hr at room temperature and revealed with SuperSignal West Femto Chemiluminescent Substrate using ImageQuant LAS4000. Stripping to ensure equal loading was done with ReBlot Plus Strong Antibody Stripping Solution (EMD Millipore 2504). All quantifications were done with ImageJ densitometry analysis.

## In vitro cell culture

HEK 293T cells were grown to 100% confluence in 75 or 150 cm<sup>2</sup> flasks, dissociated, and resuspended with TrypLE, transferred to 15 ml falcon tubes, centrifuged for 5 min at 1000 rpm at room temperature, and washed three times in Dulbecco's modified PBS (DPBS, Gibco). Cells were incubated in suspension with 1 mg/ml of biotin-beta-alanine in 10 ml of DPBS at 4°C with gentle rotation. Cells were washed three times in DPBS, pelleted by centrifugation, and frozen on dry ice. The biotinylated cell pellets were homogenized in RIPA buffer containing 1% NP40, 0.5% sodium deoxycholate, 0.1% SDS, 150 mM NaCl, 1 mM EDTA, and 25 mM TrisHCl, pH 7.4. Lysates were rotated at 4°C for 30 min and centrifuged at 10,000 g for 10 min at 4°C to remove DNA and cell debris. After measuring the protein concentration using the DC Protein Assay Kit II (Bio-Rad), the lysates were aliquoted by transferring 1–2 mg of protein to 2 ml eppendorf tubes.

## Mass spectrometry

Soluble peptides were pressure-loaded onto a 250 µm i.d. capillary with a kasil frit containing 2 cm of 10 µm Jupiter C18-A material (Phenomenex) followed by 2 cm, 5 µm Partisphere strong cation exchanger (Whatman). This column was washed with Buffer A after loading. A 100 µm i.d. capillary with a 5 µm pulled tip packed with 15 cm, 4 µm Jupiter C<sub>18</sub> material (Phenomenex) was attached to the loading column with a union and the entire split-column (loading column–union–analytical column) was placed in line with an Agilent 1100 quaternary HPLC (Palo Alto, Santa Clara, CA). For transportome analysis, the sample was analyzed using a modified four-step separation described previously (*Washburn et al., 2001*). The buffer solutions used were 5% acetonitrile/0.1% formic acid (Buffer A), 80% acetonitrile/0.1% formic acid (Buffer B), and 500 mM ammonium acetate/5% acetonitrile/0.1% formic acid (Buffer C). Step 1 consisted of a 35 min gradient from 0% to 55% Buffer B, a 5 min gradient from 55% to 70% Buffer B, 10 min 100% Buffer B and 27 min 100% Buffer A. Steps 2–3 had the following profile: 5 min of x% Buffer C with (100x)% buffer A, a 10 min Buffer A, a 5 min gradient from 0% to 15% Buffer B, a 70 min gradient from 15% to 55% Buffer B, a 5 min gradient from 55% to 100% Buffer B, a 5 min 100% Buffer B, and 20 min 100% Buffer A. The Buffer C percentages (X) were 10 and 40 for the steps 2–3, respectively. In the last step, the gradient contained: 5 min of 90% Buffer C with 10% Buffer B, a 10 min Buffer A, a 5 min gradient from 0% to 15% Buffer B, a 70 min gradient from 15% to 55% Buffer B, a 5 min gradient from 55% to 100% Buffer B, a 5 min 100% Buffer B, and 20 min 100% Buffer A. For whole proteome analysis, the sample was analyzed using a 11-step separation exactly described as above except the Buffer C percentages (X) were 10%, 15%, 20%, 30%, 40%, 50%, 60%, and 80% for the steps 2–9, respectively. In the last two steps (i.e. 10 and 11), the gradient contained: 1 min 100% Buffer A, 5 min of 100% Buffer C, a 5 min Buffer A, a 5 min gradient from 0% to 15% Buffer B, 70 min gradient from 15% to 55% Buffer B, 5 min gradient from 0% to 10% Buffer B, 75 min gradient from 10% to 45% Buffer B, 10 min 100% Buffer B, and 10 min 100% Buffer A. As peptides eluted from the microcapillary column, they were electrosprayed directly into a Velos mass spectrometer (Thermo Fisher) with the application of a distal 2.4 kV spray voltage. A cycle of one full-scan FT mass spectrum (300–2000 m/z) at 60,000 resolution followed by 20 data-dependent IT MS/MS spectra at a 35% normalized collision energy was repeated continuously throughout each step of the multidimensional separation. Application of mass spectrometer scan functions and HPLC solvent gradients were controlled by the Xcalibur data system.

## MS data analysis

MS2 (tandem mass spectra) was extracted from the XCalibur data system format (.RAW) into MS1 and MS2 formats using in-house software (RAW\_Xtractor) (*McDonald et al., 2004*). MS2 remaining after filtering were searched with ProLucid (*Xu et al., 2015*) against the UniProt\_rat\_03-25-2014 or UniProt\_mouse\_20170219\_04-17-2017 concatenated to a decoy database in which the sequence for each entry in the original database was reversed (*Cociorva et al., 2007; Peng et al., 2002*). All searches were parallelized and performed on a Beowulf computer cluster consisting of 100 1.2 GHz Athlon CPUs (*Sadygov et al., 2002*). No enzyme specificity was considered for any search. For NHS-biotin samples, the following modifications were searched for analysis for transportome analyses: a static modification of 57.02146 on cysteine for all analyses, a differential modification of 226.0776 on lysine for modified peptides. For AHA samples, the following modifications were searched: a static modification of 57.02146 on cysteine for all analyses, a differential modification of 523.2749 on methionine

for AHA to detect the standard biotin-alkyne, and a differential modification of 351.1774 (heavy) and 347.1702 (light) on methionine to detect the different AHA isotope biotin-alkynes. ProLuCID results were assembled and filtered using the DTASelect (version 2.0) program (Tabb et al., 2002; Cociorva et al., 2007). DTASelect 2.0 uses a linear discriminant analysis to dynamically set XCorr and DeltaCN thresholds for the entire dataset to achieve a user-specified false discovery rate (FDR). In DTASelect, the modified peptides were required to be partially tryptic, less than 10 ppm deviation from peptide match, and an FDR at the protein level of 0.01. The FDRs are estimated by the program from the number and quality of spectral matches to the decoy database. For all datasets, the protein FDR was <1% and the peptide FDR was <1%.

The Datasets from 'Control Rat Transportome', 'Optic Nerve Crush Rat Transportome', 'Control Mouse Transportome', and 'Kif5a KO Mouse Transportome' are composed of the total detected biotinylated proteins in 3, 3, 2, and 3 individual MS runs, respectively. Each sample was prepared by pooling tissue from 8 to 10 rats or 18 to 20 mice. NSAF was exported per UniProt accession ID for further quantitative analysis. Quantification was done using label-free analysis comparing spectral count in the different experimental groups with the Identification\_STAT\_COMPARE tool from IP2 software.

## Human and mouse retina dissociation and scRNA-seq

We analyzed a subset of recently published data (Getter et al., 2019; Hoang et al., 2020; Lu et al., 2020) which may be referenced for a more complete methodology.

Briefly, for tissue dissection and cell dissociation, a human globe from an 86-year-old Caucasian female who died of a myocardial infarction and had no known ocular disease other than cataracts was obtained from the Alabama Eye Bank (Birmingham, AL) and processed within 3.3 hr after death. The study was approved by the Johns Hopkins Institutional Review Board. The neural retina and RPE/choroid were dissected from the globe in ice-cold PBS. First, a circular incision was made on the sclera, behind the limbus, to remove the anterior parts, lens, and vitreous body. The neural retina was then peeled off from the eyecup and dissociated using the Papain Dissociation System (Worthington) following the manufacturer's instructions. RPE cells were dissociated from the eyecup by incubating with 2 ml of 0.05% EDTA (Thermo Fisher Scientific) for 20 min at 37°C. Dissociated cells were resuspended in ice-cold PBS, 0.04% BSA, and 0.5 units/ $\mu$ l RNase inhibitors.

CD1 mice between 7 and 9 weeks of age were purchased from Charles River Laboratories (Wilmington, MA). All experimental procedures were pre-approved by the institutional animal care and use committee of the Johns Hopkins University School of Medicine. Mice were euthanized, and eye globes were removed and incubated in ice-cold PBS. Retinas were dissected, and cells were dissociated using the Papain Dissociation System. In total, four biological replicates were used for the mouse scRNA study. Each replicate contained four retinas from each of two male and two female mice. Dissociated cells were resuspended in ice-cold PBS, 0.04% BSA, and 0.5 units/ $\mu$ l RNase inhibitors. Cell count and viability were assessed by trypan blue staining.

For scRNA-seq, dissociated cells (~10,000) were loaded into a 10 $\times$  Genomics Chromium Single Cell system (10 $\times$  Genomics, CA) using v2 chemistry following the manufacturer's instructions (Zheng et al., 2017). Libraries were pooled and sequenced on Illumina NextSeq with ~200 million reads per library. Sequencing results were processed through the Cell Ranger 2.1.1 pipeline (10 $\times$  Genomics) with default parameters. Seurat version 2.3.1 (Butler et al., 2018) was used to perform downstream analysis following the standard pipeline using cells with more than 200 genes and 1000 UMI counts, resulting in 16,659 mouse cells and 14,286 human cells. Samples were aggregated, and cell clusters were annotated based on previous literature (Kiser et al., 2019). A t-distributed stochastic neighbor-embedding dimension reduction was performed on the top principal components learned from high variance genes. Mclust version 5.4 was used to cluster cells in the t-distributed stochastic neighbor-embedding space, at which point cell type identity of clusters was assigned based on the expression of known marker genes for either retinal or nonretinal tissue.

## Mitochondrial tracking in RGCs

RGCs were purified from litters of E18 rats or mice as described previously (Moore et al., 2009). RGCs were seeded in low density as 2000 cells/cm<sup>2</sup> on  $\mu$ -dish 35 mm (Ibidi) in definite media: Neurobasal (Life Technologies) supplemented with penicillin-streptomycin (100 U/ml; Sigma-Aldrich Corp.), insulin

(5 µg/ml; Sigma-Aldrich Corp.), sodium pyruvate (1 mM; Sigma-Aldrich Corp.), L-glutamine (1 mM; Sigma-Aldrich Corp.), triiodothyronine (T3; 40 ng/ml; Sigma-Aldrich Corp.), N-acetyl cysteine (5 mg/ml; Sigma-Aldrich Corp.), B-27 Supplement (Gibco), Sato Supplement (1 µg/ml transferrin, 1 µg/ml BSA, 2 nM progesterone, 0.16 µg/ml putrescine, and 0.4 ng/ml sodium selenite), brain-derived neurotrophic factor (BDNF; 50 ng/ml; Peprotech, Rocky Hill, NJ), CTNF (10 ng/ml; Peprotech), forskolin (5 nM; Sigma-Aldrich Corp.), and basic fibroblast growth factor (10 ng/ml; Peprotech). After 24 hr, Kif5a or anti-Kif5a shRNA were transduced by AAV vector into the cultured RGCs (gift of Dr Sui Wang). After 5 days on the dish, mitochondria were labeled with 50 nM of MitoTracker Deep Red FM (Invitrogen) for 15 min and imaged every 1.5 s for 3 min by confocal microscope with incubation (LSM880, Zeiss). From the time-lapse images, we generated kymograph using ImageJ 'Multiple Kymograph' plug-in for ImageJ submitted by J Rietdorf and A Seitz (European Molecular Biology Laboratory, Heidelberg, Germany) to categorize mitochondrial state (stopped, fluttering, anterograde, and retrograde transport) and calculate speed of the transport as described previously (Yokota *et al.*, 2015).

### Protein-protein interaction analysis

All proteins labeled in **Figure 3e** plus Kif5a were input into STRINGdb (<http://string-db.org>) (Szklarczyk *et al.*, 2017). Interactions sources included: textmining, experiments, databases, co-expression, neighborhood, gene fusion, and co-occurrence, with a medium 0.400 required interaction score. These data were exported into Cytoscape 3.7 for graphical organization.

### Statistical analysis

Data were analyzed using R version 3.5.0 (The R Foundation for Statistical Computing) or Graphpad Prism 7 (GraphPad, San Diego, CA). For correlation between proteomic samples, significance testing used Pearson's correlation coefficient in package 'GGally'. Quantitative proteomic comparisons of individual proteins were made using the 't-test' function of the 'limma' package in R. For statistical comparison of Kif5a transport after optic nerve crush by western blot, a one-sample, two-sided t-test was used. For all other comparisons between two samples, two-sided unpaired t-tests were used. For group comparisons, ordinary one-way ANOVA with post-hoc Sidak correction was used.

### Acknowledgements

This work was supported by the NIH: EY011261, EY027437, P30 EY019005, R01MH103134, and the Hahn Family Foundation to HTC, P41 GM103533 and R01MH067880 to JRY, P30 EY026877, the Glaucoma Research Foundation and Research to Prevent Blindness to JLG, and U01EY027261 to JLG, JRY, and HTC.

## Additional information

### Funding

Funder	Grant reference number	Author
National Institutes of Health	EY011261	Hollis T Cline
National Institutes of Health	EY027437	Hollis T Cline
National Institutes of Health	P30 EY019005	Hollis T Cline
National Institutes of Health	R01MH103134	Hollis T Cline
National Institutes of Health	P41 GM103533	John R Yates
Hahn Family Foundation		Hollis T Cline

Funder	Grant reference number	Author
National Institutes of Health	R01MH067880	John R Yates
National Institutes of Health	P30 EY026877	Jeffrey L Goldberg
Glaucoma Research Foundation		Jeffrey L Goldberg
Research to Prevent Blindness		Jeffrey L Goldberg
National Institutes of Health	U01EY027261	John R Yates Hollis T Cline Jeffrey L Goldberg

The funders had no role in study design, data collection and interpretation, or the decision to submit the work for publication.

### Author contributions

Sahil H Shah, Conceptualization, Data curation, Formal analysis, Funding acquisition, Investigation, Methodology, Software, Validation, Visualization, Writing – original draft, Writing – review and editing; Lucio M Schiapparelli, Conceptualization, Data curation, Formal analysis, Investigation, Methodology, Validation, Writing – review and editing; Yuanhui Ma, Conceptualization, Data curation, Formal analysis, Investigation, Methodology, Resources, Visualization; Satoshi Yokota, Data curation, Formal analysis, Investigation, Methodology, Visualization; Melissa Atkins, Formal analysis, Investigation, Methodology, Visualization; Xin Xia, Investigation, Methodology, Validation; Evan G Cameron, Conceptualization, Investigation, Methodology; Thanh Huang, Data curation, Formal analysis, Investigation, Methodology, Resources, Visualization; Sarah Saturday, Formal analysis, Investigation, Methodology; Catalina B Sun, Data curation, Investigation, Methodology, Visualization; Cara Knasel, Investigation, Methodology, Visualization; Seth Blackshaw, Data curation, Project administration, Resources, Supervision, Visualization; John R Yates, Funding acquisition, Methodology, Project administration, Resources, Supervision, Validation; Hollis T Cline, Conceptualization, Funding acquisition, Methodology, Project administration, Resources, Supervision, Writing – review and editing; Jeffrey L Goldberg, Conceptualization, Formal analysis, Funding acquisition, Methodology, Project administration, Resources, Supervision, Writing – review and editing

### Author ORCIDs

Sahil H Shah  <http://orcid.org/0000-0002-6601-219X>  
 Satoshi Yokota  <http://orcid.org/0000-0002-3727-7279>  
 Seth Blackshaw  <http://orcid.org/0000-0002-1338-8476>  
 John R Yates  <http://orcid.org/0000-0001-5267-1672>  
 Hollis T Cline  <http://orcid.org/0000-0002-4887-9603>  
 Jeffrey L Goldberg  <http://orcid.org/0000-0002-1390-7360>

### Ethics

All animal experiments conformed to the ARVO statement for the Use of Animals in Ophthalmic and Vision Research and were reviewed and approved by the Institutional Animal Care and Use Committee (IACUC) and the Institutional Biosafety Committee of University of California, San Diego, Scripps Research, and Stanford University.

### Decision letter and Author response

Decision letter <https://doi.org/10.7554/eLife.68148.sa1>  
 Author response <https://doi.org/10.7554/eLife.68148.sa2>

## Additional files

### Supplementary files

- Transparent reporting form

**Data availability**

All data generated during this study are included in the manuscript and supporting source files in excel format. Source data files have been provided for Figures 1, 4, 5 and Figure Supplement 2.

The following previously published datasets were used:

Author(s)	Year	Dataset title	Dataset URL	Database and Identifier
Blackshaw S, Clark BS, Handa JT, Bremner R, Zack DJ	2020	scRNA-seq of the developing human retina	<a href="https://www.ncbi.nlm.nih.gov/geo/query/acc.cgi?acc=GSE138002">https://www.ncbi.nlm.nih.gov/geo/query/acc.cgi?acc=GSE138002</a>	NCBI Gene Expression Omnibus, GSE138002
Hoang T, Wang J, Boyd P, Wang F, Hyde DR, Qian J, Blackshaw S	2020	Comparative transcriptomic and epigenomic analysis identifies key regulators of injury response and neurogenic competence in retinal glia	<a href="https://www.ncbi.nlm.nih.gov/geo/query/acc.cgi?acc=GSE135406">https://www.ncbi.nlm.nih.gov/geo/query/acc.cgi?acc=GSE135406</a>	NCBI Gene Expression Omnibus, GSE135406

**References**

- Ahmed BY**, Chakravarthy S, Eggers R, Hermens W, Zhang JY, Niclou SP, Levelt C, Sablitzky F, Anderson PN, Lieberman AR, Verhaagen J. 2004. Efficient delivery of Cre-recombinase to neurons in vivo and stable transduction of neurons using adeno-associated and lentiviral vectors *BMC Neuroscience* **5**:4. DOI: <https://doi.org/10.1186/1471-2202-5-4>, PMID: 15005815
- Anderson DR**, Hendrickson A. 1974. Effect of intraocular pressure on rapid axoplasmic transport in monkey optic nerve *Investigative Ophthalmology* **13**:771–783 PMID: 4137635.
- Belin S**, Nawabi H, Wang C, Tang S, Latremoliere A, Warren P, Schorle H, Uncu C, Woolf CJ, He Z, Steen JA. 2015. Injury-induced decline of intrinsic regenerative ability revealed by quantitative proteomics *Neuron* **86**:1000–1014. DOI: <https://doi.org/10.1016/j.neuron.2015.03.060>, PMID: 25937169
- Brenner D**, Yilmaz R, Müller K, Grehl T, Petri S, Meyer T, Grosskreutz J, Weydt P, Ruf W, Neuwirth C, Weber M, Pinto S, Claeys KG, Schrank B, Jordan B, Knehr A, Günther K, Hübers A, Zeller D, Kubisch C, et al. 2018. Hot-spot KIF5A mutations cause familial ALS *Brain : A Journal of Neurology* **141**:688–697. DOI: <https://doi.org/10.1093/brain/awx370>, PMID: 29342275
- Butler A**, Hoffman P, Smibert P, Papalexli E, Satija R. 2018. Integrating single-cell transcriptomic data across different conditions, technologies, and species *Nature Biotechnology* **36**:411–420. DOI: <https://doi.org/10.1038/nbt.4096>, PMID: 29608179
- Butowt R**, von Bartheld CS. 2007. Conventional kinesin-I motors participate in the anterograde axonal transport of neurotrophins in the visual system *Journal of Neuroscience Research* **85**:2546–2556. DOI: <https://doi.org/10.1002/jnr.21165>, PMID: 17243173
- Cai D**, Shen Y, De Bellard M, Tang S, Filbin MT. 1999. Prior exposure to neurotrophins blocks inhibition of axonal regeneration by MAG and myelin via a cAMP-dependent mechanism *Neuron* **22**:89–101. DOI: [https://doi.org/10.1016/s0896-6273\(00\)80681-9](https://doi.org/10.1016/s0896-6273(00)80681-9), PMID: 10027292
- Cai D**, Hoppe AD, Swanson JA, Verhey KJ. 2007. Kinesin-1 structural organization and conformational changes revealed by FRET stoichiometry in live cells *The Journal of Cell Biology* **176**:51–63. DOI: <https://doi.org/10.1083/jcb.200605097>, PMID: 17200416
- Campbell PD**, Shen K, Sapio MR, Glenn TD, Talbot WS, Marlow FL. 2014. Unique function of Kinesin Kif5A in localization of mitochondria in axons *The Journal of Neuroscience* **34**:14717–14732. DOI: <https://doi.org/10.1523/JNEUROSCI.2770-14.2014>, PMID: 25355224
- Cartoni R**, Norsworthy MW, Bei F, Wang C, Li S, Zhang Y, Gabel CV, Schwarz TL, He Z. 2016. The Mammalian-Specific Protein Armcx1 Regulates Mitochondrial Transport during Axon Regeneration *Neuron* **92**:1294–1307. DOI: <https://doi.org/10.1016/j.neuron.2016.10.060>, PMID: 28009275
- Chen Y**, Sheng ZH. 2013. Kinesin-1-syntrophin coupling mediates activity-dependent regulation of axonal mitochondrial transport *The Journal of Cell Biology* **202**:351–364. DOI: <https://doi.org/10.1083/jcb.201302040>, PMID: 23857772
- Chevalier-Larsen E**, Holzbaur ELF. 2006. Axonal transport and neurodegenerative disease *Biochimica et Biophysica Acta* **1762**:1094–1108. DOI: <https://doi.org/10.1016/j.bbadis.2006.04.002>, PMID: 16730956
- Chou TH**, Toft-Nielsen J, Porciatti V. 2018. High-Throughput Binocular Pattern Electroretinograms in the Mouse *Methods in Molecular Biology (Clifton, N.J.)* **1695**:63–68. DOI: [https://doi.org/10.1007/978-1-4939-7407-8\\_6](https://doi.org/10.1007/978-1-4939-7407-8_6), PMID: 29190018
- Cociorva D**, L Tabb D, Yates JR. 2007. Validation of Tandem Mass Spectrometry Database Search Results Using DTASelect *Current Protocols in Bioinformatics Chapter 13*:Unit. DOI: <https://doi.org/10.1002/0471250953.bi1304s16>, PMID: 18428785
- Deshaies J-E**, Shkreta L, Moszczynski AJ, Sidibé H, Semmler S, Fouillen A, Bennett ER, Bekenstein U, Destroismaisons L, Toutant J, Delmotte Q, Volkening K, Stabile S, Aulas A, Khalfallah Y, Soreq H, Nanci A, Strong MJ, Chabot B, Vande Velde C. 2018. TDP-43 regulates the alternative splicing of hnRNP A1 to yield an



- aggregation-prone variant in amyotrophic lateral sclerosis *Brain* **141**:1320–1333. DOI: <https://doi.org/10.1093/brain/awy062>, PMID: 29562314
- Dieterich DC**, Hodas JJJ, Gouzer G, Shadrin IY, Ngo JT, Triller A, Tirrell DA, Schuman EM. 2010. In situ visualization and dynamics of newly synthesized proteins in rat hippocampal neurons *Nature Neuroscience* **13**:897–905. DOI: <https://doi.org/10.1038/nn.2580>, PMID: 20543841
- Galvao J**, Iwao K, Apará A, Wang Y, Ashouri M, Shah TN, Blackmore M, Kunzevitzky NJ, Moore DL, Goldberg JL. 2018. The Kruppel-Like Factor Gene Target *Dusp14* Regulates Axon Growth and Regeneration *Investigative Ophthalmology & Visual Science* **59**:2736–2747. DOI: <https://doi.org/10.1167/iovs.17-23319>, PMID: 29860460
- Getter T**, Suh S, Hoang T, Handa JT, Dong Z, Ma X, Chen Y, Blackshaw S, Palczewski K. 2019. The selective estrogen receptor modulator raloxifene mitigates the effect of all-trans-retinal toxicity in photoreceptor degeneration *The Journal of Biological Chemistry* **294**:9461–9475. DOI: <https://doi.org/10.1074/jbc.RA119.008697>, PMID: 31073029
- Gilley J**, Orsomando G, Nascimento-Ferreira I, Coleman MP. 2015. Absence of SARM1 Rescues Development and Survival of NMNAT2-Deficient Axons *Cell Reports* **10**:1974–1981. DOI: <https://doi.org/10.1016/j.celrep.2015.02.060>, PMID: 25818290
- Glater EE**, Megeath LJ, Stowers RS, Schwarz TL. 2006. Axonal transport of mitochondria requires mltin to recruit kinesin heavy chain and is light chain independent *The Journal of Cell Biology* **173**:545–557. DOI: <https://doi.org/10.1083/jcb.200601067>, PMID: 16717129
- Gumy LF**, Katrukha EA, Grigoriev I, Jaarsma D, Kapitein LC, Akhmanova A, Hoogenraad CC, Gumy LF, Katrukha EA, Grigoriev I, Jaarsma D, Kapitein LC, Akhmanova A. 2017. MAP2 Defines a Pre-axonal Filtering Zone to Regulate KIF1- versus KIF5-Dependent Cargo Transport in Sensory Neurons *Neuron* **94**:347–362. DOI: <https://doi.org/10.1016/j.neuron.2017.03.046>, PMID: 28426968
- Han SM**, Baig HS, Hammarlund M. 2016. Mitochondria Localize to Injured Axons to Support Regeneration *Neuron* **92**:1308–1323. DOI: <https://doi.org/10.1016/j.neuron.2016.11.025>, PMID: 28009276
- Hendricks AG**, Perlson E, Ross JL, Schroeder HW, Tokito M, Holzbaur ELF. 2010. Motor Coordination via a Tug-of-War Mechanism Drives Bidirectional Vesicle Transport *Current Biology* **20**:697–702. DOI: <https://doi.org/10.1016/j.cub.2010.02.058>, PMID: 20399099
- Hinz FI**, Dieterich DC, Tirrell DA, Schuman EM. 2012. Noncanonical amino acid labeling in vivo to visualize and affinity purify newly synthesized proteins in larval zebrafish *ACS Chemical Neuroscience* **3**:40–49. DOI: <https://doi.org/10.1021/cn2000876>, PMID: 22347535
- Hirokawa N**, Noda Y, Tanaka Y, Niwa S. 2009. Kinesin superfamily motor proteins and intracellular transport *Nature Reviews. Molecular Cell Biology* **10**:682–696. DOI: <https://doi.org/10.1038/nrm2774>, PMID: 19773780
- Hoang T**, Wang J, Boyd P, Wang F, Santiago C, Jiang L, Yoo S, Lahne M, Todd LJ, Jia M, Saez C, Keuthan C, Palazzo I, Squires N, Campbell WA, Rajaii F, Parayil T, Trinh V, Kim DW, Wang G, et al. 2020. Gene regulatory networks controlling vertebrate retinal regeneration *Science (New York, N.Y.)* **370**:eabb8598. DOI: <https://doi.org/10.1126/science.abb8598>, PMID: 33004674
- Hulce JJ**, Cognetta AB, Niphakis MJ, Tully SE, Cravatt BF. 2013. Proteome-wide mapping of cholesterol-interacting proteins in mammalian cells *Nature Methods* **10**:259–264. DOI: <https://doi.org/10.1038/nmeth.2368>, PMID: 23396283
- Ishida M**, Ohbayashi N, Fukuda M. 2015. Rab1A regulates anterograde melanosome transport by recruiting kinesin-1 to melanosomes through interaction with SKIP *Scientific Reports* **5**:8238. DOI: <https://doi.org/10.1038/srep08238>, PMID: 25649263
- Kanai Y**, Dohmae N, Hirokawa N. 2004. Kinesin transports RNA: Isolation and characterization of an RNA-transporting granule *Neuron* **43**:513–525. DOI: <https://doi.org/10.1016/j.neuron.2004.07.022>, PMID: 15312650
- Kim HJ**, Kim NC, Wang Y-D, Scarborough EA, Moore J, Diaz Z, MacLea KS, Freibaum B, Li S, Molliex A, Kanagaraj AP, Carter R, Boylan KB, Wojtas AM, Rademakers R, Pinkus JL, Greenberg SA, Trojanowski JQ, Traynor BJ, Smith BN, et al. 2013. Mutations in prion-like domains in hnRNPA2B1 and hnRNPA1 cause multisystem proteinopathy and ALS *Nature* **495**:467–473. DOI: <https://doi.org/10.1038/nature11922>, PMID: 23455423
- Kiser PD**, Kolesnikov AV, Kiser JZ, Dong Z, Chaurasia B, Wang L, Summers SA, Hoang T, Blackshaw S, Peachey NS, Kefalov VJ, Palczewski K. 2019. Conditional deletion of *Des1* in the mouse retina does not impair the visual cycle in cones *FASEB Journal* **33**:5782–5792. DOI: <https://doi.org/10.1096/fj.201802493R>, PMID: 30645148
- Knöferle J**, Koch JC, Ostendorf T, Michel U, Planchamp V, Vutova P, Tönges L, Stadelmann C, Brück W, Bähr M, Lingor P. 2010. Mechanisms of acute axonal degeneration in the optic nerve in vivo *PNAS* **107**:6064–6069. DOI: <https://doi.org/10.1073/pnas.0909794107>, PMID: 20231460
- Lachke SA**, Alkuraya FS, Kneeland SC, Ohn T, Aboukhalil A, Howell GR, Saadi I, Cavalleco R, Yue Y, Tsai AC-H, Nair KS, Cosma MI, Smith RS, Hodges E, Alfadhli SM, Al-Hajeri A, Shamseldin HE, Behbehani A, Hannon GJ, Bulyk ML, et al. 2011. Mutations in the RNA Granule Component TDRD7 Cause Cataract and Glaucoma *Science (New York, N.Y.)* **331**:1571–1576. DOI: <https://doi.org/10.1126/science.1195970>, PMID: 21436445
- Leaver SG**, Cui Q, Plant GW, Arulpragasam A, Hisheh S, Verhaagen J, Harvey AR. 2006. AAV-mediated expression of CNTF promotes long-term survival and regeneration of adult rat retinal ganglion cells *Gene Therapy* **13**:1328–1341. DOI: <https://doi.org/10.1038/sj.gt.3302791>, PMID: 16708079
- Leon S**, Yin Y, Nguyen J, Irwin N, Benowitz LI. 2000. Lens injury stimulates axon regeneration in the mature rat optic nerve *The Journal of Neuroscience* **20**:4615–4626. PMID: 10844031.
- Liddelow SA**, Guttenplan KA, Clarke LE, Bennett FC, Bohlen CJ, Schirmer L, Bennett ML, Münch AE, Chung W-S, Peterson TC, Wilton DK, Frouin A, Napier BA, Panicker N, Kumar M, Buckwalter MS, Rowitch DH,

- Dawson VL, Dawson TM, Stevens B, et al. 2017. Neurotoxic reactive astrocytes are induced by activated microglia *Nature* **541**:481–487. DOI: <https://doi.org/10.1038/nature21029>, PMID: 28099414
- Liu H-H, Bui BV, Nguyen CTO, Kezic JM, Vingrys AJ, He Z. 2015. Chronic ocular hypertension induced by circumlimbal suture in rats *Investigative Ophthalmology & Visual Science* **56**:2811–2820. DOI: <https://doi.org/10.1167/iovs.14-16009>, PMID: 25829414
- Loschi M, Leishman CC, Berardone N, Boccaccio GL. 2009. Dynein and kinesin regulate stress-granule and P-body dynamics *Journal of Cell Science* **122**:3973–3982. DOI: <https://doi.org/10.1242/jcs.051383>, PMID: 19825938
- Lu Y, Shiao F, Yi W, Lu S, Wu Q, Pearson JD, Kallman A, Zhong S, Hoang T, Zuo Z, Zhao F, Zhang M, Tsai N, Zhuo Y, He S, Zhang J, Stein-O'Brien GL, Sherman TD, Duan X, Fertig EJ, et al. 2020. Single-Cell Analysis of Human Retina Identifies Evolutionarily Conserved and Species-Specific Mechanisms Controlling Development *Developmental Cell* **53**:473–491. DOI: <https://doi.org/10.1016/j.devcel.2020.04.009>, PMID: 32386599
- Macaskill AF, Rinholm JE, Twelvetrees AE, Arancibia-Carcamo IL, Muir J, Fransson A, Aspenstrom P, Attwell D, Kittler JT. 2009. Miro1 Is a Calcium Sensor for Glutamate Receptor-Dependent Localization of Mitochondria at Synapses *Neuron* **61**:541–555. DOI: <https://doi.org/10.1016/j.neuron.2009.01.030>, PMID: 19249275
- McClatchy DB, Ma Y, Liu C, Stein BD, Martínez-Bartolomé S, Vasquez D, Hellberg K, Shaw RJ, Yates JR. 2015. Pulsed azidohomoalanine labeling in mammals (PALM) detects changes in liver-specific LKB1 knockout mice *Journal of Proteome Research* **14**:4815–4822. DOI: <https://doi.org/10.1021/acs.jproteome.5b00653>, PMID: 26445171
- McDonald WH, Tabb DL, Sadygov RG, MacCoss MJ, Venable J, Graumann J, Johnson JR, Cociorva D, Yates JR. 2004. MS1, MS2, and SQT - Three unified, compact, and easily parsed file formats for the storage of shotgun proteomic spectra and identifications *Rapid Communications in Mass Spectrometry* **18**:2162–2168. DOI: <https://doi.org/10.1002/rcm.1603>, PMID: 15317041
- McKerracher L, Vidal-Sanz M, Essagian C, Aguayo AJ. 1990. Selective impairment of slow axonal transport after optic nerve injury in adult rats *The Journal of Neuroscience* **10**:2834–2841 PMID: 1696983.
- Michaevlevski I, Medzihradsky KF, Lynn A, Burlingame AL, Fainzilber M. 2010. Axonal transport proteomics reveals mobilization of translation machinery to the lesion site in injured sciatic nerve *Molecular & Cellular Proteomics* **9**:976–987. DOI: <https://doi.org/10.1074/mcp.M900369-MCP200>, PMID: 19955087
- Milosevic I, Giovedi S, Lou X, Raimondi A, Collesi C, Shen H, Paradise S, O'Toole E, Ferguson S, Cremona O, De Camilli P. 2011. Recruitment of endophilin to clathrin-coated pit necks is required for efficient vesicle uncoating after fission *Neuron* **72**:587–601. DOI: <https://doi.org/10.1016/j.neuron.2011.08.029>, PMID: 22099461
- Minckler DS, Bunt AH, Johanson GW. 1977. Orthograde and retrograde axoplasmic transport during acute ocular hypertension in the monkey *Investig Ophthalmol Vis Sci* **16**:426–441.
- Molliex A, Temirov J, Lee J, Coughlin M, Kanagaraj AP, Kim HJ, Mittag T, Taylor JP. 2015. Phase Separation by Low Complexity Domains Promotes Stress Granule Assembly and Drives Pathological Fibrillization *Cell* **163**:123–133. DOI: <https://doi.org/10.1016/j.cell.2015.09.015>, PMID: 26406374
- Moore DL, Blackmore MG, Hu Y, Kaestner KH, Bixby JL, Lemmon VP, Goldberg JL. 2009. KLF Family Members Regulate Intrinsic Axon Regeneration Ability *Science (New York, N.Y.)* **326**:298–301. DOI: <https://doi.org/10.1126/science.1175737>, PMID: 19815778
- Morfini G, Szebenyi G, Richards B, Brady ST. 2001. Regulation of kinesin: Implications for neuronal development *Developmental Neuroscience* **23**:364–376. DOI: <https://doi.org/10.1159/000048720>, PMID: 11756752
- Morfini GA, Burns M, Binder LI, Kanaan NM, LaPointe N, Bosco DA, Brown RH, Brown H, Tiwari A, Hayward L, Edgar J, Nave KA, Garberrn J, Atagi Y, Song Y, Pigino G, Brady ST. 2009. Axonal transport defects in neurodegenerative diseases *The Journal of Neuroscience* **29**:12776–12786. DOI: <https://doi.org/10.1523/JNEUROSCI.3463-09.2009>, PMID: 19828789
- Nakajima K, Yin X, Takei Y, Seog D-H, Homma N, Hirokawa N. 2012. Article Molecular Motor KIF5A Is Essential for GABA A Receptor Transport, and KIF5A Deletion Causes Epilepsy *Neuron* **76**:945–961. DOI: <https://doi.org/10.1016/j.neuron.2012.10.012>, PMID: 23217743
- Nicolas A, Kenna KP, Renton AE, Ticozzi N, Faghri F, Chia R, Dominov JA, Kenna BJ, Nalls MA, Keagle P, Rivera AM, van Rheenen W, Murphy NA, van Vugt J, Geiger JT, Van der Spek RA, Pliner HA, Smith BN, Marangi G, Topp SD, et al. 2018. Genome-wide Analyses Identify KIF5A as a Novel ALS Gene *Neuron* **97**:1268–1283. DOI: <https://doi.org/10.1016/j.neuron.2018.02.027>, PMID: 29566793
- Oh JY, Kwon A, Jo A, Kim H, Goo YS, Lee JA, Kim HK. 2013. Activity-dependent synaptic localization of processing bodies and their role in dendritic structural plasticity. *Journal of Cell Science* **126**:2114–2123. DOI: <https://doi.org/10.1242/jcs.125690>, PMID: 23487039
- Park KK, Liu K, Hu Y, Kanter JL, He Z. 2010. PTEN/mTOR and axon regeneration *Experimental Neurology* **223**:45–50. DOI: <https://doi.org/10.1016/j.expneurol.2009.12.032>, PMID: 20079353
- Peng JM, Elias JE, Thoreen CC, Licklider LJ, Gygi SP. 2002. Evaluation of multidimensional chromatography coupled with tandem mass spectrometry (LC/LC-MS) for Large-Scale Protein Analysis: The Yeast Proteome *Journal of Proteome Research* **2**:43–50. DOI: <https://doi.org/10.1021/pr025556v>, PMID: 12643542
- Quigley HA, Anderson DR. 1977. Distribution of axonal transport blockade by acute intraocular pressure elevation in the primate optic nerve head *Investig Ophthalmol Vis Sci* **16**:640–644.
- Quigley HA, Guy J, Anderson DR. 1979. Blockade of Rapid Axonal Transport: Effect of Intraocular Pressure Elevation in Primate Optic Nerve *Archives of Ophthalmology (Chicago, Ill)* **97**:525–531. DOI: <https://doi.org/10.1001/archophth.1979.01020010269018>, PMID: 84662

- Rahman A**, Kamal A, Roberts EA, Goldstein LSB. 1999. Defective Kinesin Heavy Chain Behavior in Mouse Kinesin Light Chain Mutants *The Journal of Cell Biology* **146**:1277–1288. DOI: <https://doi.org/10.1083/jcb.146.6.1277>, PMID: 10491391
- Reid E**, Kloos M, Ashley-Koch A, Hughes L, Bevan S, Svenson IK, Graham FL, Gaskell PC, Dearlove A, Pericak-Vance MA, Rubinsztein DC, Marchuk DA. 2002. A Kinesin Heavy Chain (KIF5A) Mutation in Hereditary Spastic Paraplegia (SPG10) *American Journal of Human Genetics* **71**:1189–1194. DOI: <https://doi.org/10.1086/344210>, PMID: 12355402
- Sadygov RG**, Eng J, Durr E, Saraf A, McDonald H, MacCoss MJ, Yates JR. 2002. Code developments to improve the efficiency of automated MS/MS spectra interpretation *Journal of Proteome Research* **1**:211–215. DOI: <https://doi.org/10.1021/pr015514r>, PMID: 12645897
- Sánchez-Migallón MC**, Valiente-Soriano FJ, Nadal-Nicolás FM, Vidal-Sanz M, Agudo-Barriuso M. 2016. Apoptotic retinal ganglion cell death after optic nerve transection or crush in mice: Delayed RGC loss with BDNF or a caspase 3 inhibitor *Investigative Ophthalmology & Visual Science* **57**:81–93. DOI: <https://doi.org/10.1167/iovs.15-17841>, PMID: 26780312
- Sato K**, Saigusa D, Saito R, Fujioka A, Nakagawa Y, Nishiguchi KM, Kokubun T, Motoike IN, Maruyama K, Omodaka K, Shiga Y, Uruno A, Koshiba S, Yamamoto M, Nakazawa T. 2018. Metabolomic changes in the mouse retina after optic nerve injury *Scientific Reports* **8**:1–13. DOI: <https://doi.org/10.1038/s41598-018-30464-z>, PMID: 30093719
- Schiapparelli LM**, McClatchy DB, Liu HH, Sharma P, Yates JR, Cline HT. 2014. Direct Detection of Biotinylated Proteins by Mass Spectrometry *Journal of Proteome Research* **13**:3966–3978. DOI: <https://doi.org/10.1021/pr5002862>, PMID: 25117199
- Schiapparelli LM**, Shah SH, Ma Y, McClatchy DB, Sharma P, Li J, Yates JR, Goldberg JL, Cline HT. 2019. The Retinal Ganglion Cell Transportome Identifies Proteins Transported to Axons and Presynaptic Compartments in the Visual System In Vivo *Cell Reports* **28**:1935–1947. DOI: <https://doi.org/10.1016/j.celrep.2019.07.037>, PMID: 31412257
- Seshadri S**, Fitzpatrick AL, Ikram MA, DeStefano AL, Gudnason V, Boada M, Bis JC, Smith AV, Carassquillo MM, Lambert JC, Harold D, Schrijvers EMC, Ramirez-Lorca R, Dobbie S, Longstreth WT Jr, Janssens ACJW, Pankratz VS, Dartigues JF, Hollingworth P, Aspelund T, et al. 2010. Genome-wide Analysis of Genetic Loci Associated with Alzheimer Disease *JAMA* **303**:1832–1840. DOI: <https://doi.org/10.1001/jama.2010.574>, PMID: 20460622
- Speers AE**, Cravatt BF. 2009. Activity-Based Protein Profiling (ABPP) and Click Chemistry (CC)-ABPP by MudPIT Mass Spectrometry *Current Protocols in Chemical Biology* **1**:29–41. DOI: <https://doi.org/10.1002/9780470559277.ch090138>, PMID: 21701697
- Szklarczyk D**, Morris JH, Cook H, Kuhn M, Wyder S, Simonovic M, Santos A, Doncheva NT, Roth A, Bork P, Jensen LJ, von Mering C. 2017. The STRING database in 2017: quality-controlled protein – protein association networks, made broadly accessible *Nucleic Acids Research* **45**:D362–D368. DOI: <https://doi.org/10.1093/nar/gkw937>, PMID: 27924014
- Tabb DL**, McDonald WH, Yates JR. 2002. DTASelect and contrast: Tools for assembling and comparing protein identifications from shotgun proteomics *Journal of Proteome Research* **1**:21–26. DOI: <https://doi.org/10.1021/pr015504q>, PMID: 12643522
- Takahara Y**, Inatani M, Eto K, Inoue T, Kreymerman A, Miyake S, Ueno S, Nagaya M, Nakanishi A, Iwao K, Takamura Y, Sakamoto H, Satoh K, Kondo M, Sakamoto T, Goldberg JL, Nabekura J, Tanihara H. 2015. In vivo imaging of axonal transport of mitochondria in the diseased and aged mammalian CNS *PNAS* **112**:10515–10520. DOI: <https://doi.org/10.1073/pnas.1509879112>, PMID: 26240337
- Tessa A**, Silvestri G, de Leva MF, Modoni A, Denora PS, Masciullo M, Dotti MT, Casali C, Melone MAB, Federico A, Filla A, Santorelli FM. 2008. A novel KIF5A/SPG10 mutation in spastic paraplegia associated with axonal neuropathy *Journal of Neurology* **255**:1090–1092. DOI: <https://doi.org/10.1007/s00415-008-0840-8>, PMID: 18500496
- Toda H**, Mochizuki H, Flores R, Josowitz R, Krasieva TB, Lamorte VJ, Suzuki E, Gindhart JG, Furukubo-Tokunaga K, Tomoda T. 2008. UNC-51/ATG1 kinase regulates axonal transport by mediating motor-cargo assembly *Genes & Development* **22**:3292–3307. DOI: <https://doi.org/10.1101/gad.1734608>, PMID: 19056884
- Wang X**, Schwarz TL. 2009. The Mechanism of Ca<sup>2+</sup>-Dependent Regulation of Kinesin-Mediated Mitochondrial Motility *Cell* **136**:163–174. DOI: <https://doi.org/10.1016/j.cell.2008.11.046>, PMID: 19135897
- Wang Y**, Cameron EG, Li J, Stiles TL, Kritzer MD, Lodhavia R, Hertz J, Nguyen T, Kapiloff MS, Goldberg JL. 2015. Muscle A-Kinase Anchoring Protein- $\alpha$  is an Injury-Specific Signaling Scaffold Required for Neurotrophic- and Cyclic Adenosine Monophosphate-Mediated Survival *EBioMedicine* **2**:1880–1887. DOI: <https://doi.org/10.1016/j.ebiom.2015.10.025>, PMID: 26844267
- Washburn MP**, Wolters D, Yates JR. 2001. Large-scale analysis of the yeast proteome by multidimensional protein identification technology *Nature Biotechnology* **19**:242–247. DOI: <https://doi.org/10.1038/85686>, PMID: 11231557
- Xia CH**, Roberts EA, Her LS, Liu X, Williams DS, Cleveland DW, Goldstein LSB. 2003. Abnormal neurofilament transport caused by targeted disruption of neuronal kinesin heavy chain KIF5A *The Journal of Cell Biology* **161**:55–66. DOI: <https://doi.org/10.1083/jcb.200301026>, PMID: 12682084
- Xu T**, Park SK, Venable JD, Wohlschlegel JA, Diedrich JK, Cociorva D, Lu B, Liao L, Hewel J, Han X, Wong CCL, Fonslow B, Delahunty C, Gao Y, Shah H, Yates JR. 2015. ProLuCID: An improved SEQUEST-like algorithm with

- enhanced sensitivity and specificity *Journal of Proteomics* **129**:16–24. DOI: <https://doi.org/10.1016/j.jprot.2015.07.001>, PMID: 26171723
- Yang R**, Bentley M, Huang C-F, Banker G. 2016. Analyzing kinesin motor domain translocation in cultured hippocampal neurons *Methods in Cell Biology* **131**:217–232. DOI: <https://doi.org/10.1016/bs.mcb.2015.06.021>, PMID: 26794516
- Yasuda M**, Tanaka Y, Omodaka K, Nishiguchi KM, Nakamura O, Tsuda S, Nakazawa T. 2016. Transcriptome profiling of the rat retina after optic nerve transection *Scientific Reports* **6**:1–11. DOI: <https://doi.org/10.1038/srep28736>, PMID: 27353354
- Yokota S**, Takihara Y, Arimura S, Miyake S, Takamura Y, Yoshimura N, Inatani M. 2015. Altered Transport Velocity of Axonal Mitochondria in Retinal Ganglion Cells After Laser-Induced Axonal Injury In Vitro *Investigative Ophthalmology & Visual Science* **56**:8019–8025. DOI: <https://doi.org/10.1167/iovs.15-17876>, PMID: 26720449
- Zhang B**, Higuchi M, Yoshiyama Y, Ishihara T, Forman MS, Martinez D, Joyce S, Trojanowski JQ, Lee VMY. 2004. Retarded axonal transport of R406W mutant tau in transgenic mice with a neurodegenerative tauopathy *The Journal of Neuroscience* **24**:4657–4667. DOI: <https://doi.org/10.1523/JNEUROSCI.0797-04.2004>, PMID: 15140937
- Zhao C**, Takita J, Tanaka Y, Setou M, Nakagawa T, Takeda S, Yang HW, Terada S, Nakata T, Takei Y, Saito M, Tsuji S, Hayashi Y, Hirokawa N. 2001. Charcot-Marie-Tooth disease type 2A caused by mutation in a microtubule motor KIF1Bbeta *Cell* **105**:587–597. DOI: [https://doi.org/10.1016/s0092-8674\(01\)00363-4](https://doi.org/10.1016/s0092-8674(01)00363-4), PMID: 11389829
- Zheng GXY**, Terry JM, Belgrader P, Ryvkin P, Bent ZW, Wilson R, Ziraldo SB, Wheeler TD, McDermott GP, Zhu J, Gregory MT, Shuga J, Montesclaros L, Underwood JG, Masquelier DA, Nishimura SY, Schnell-Levin M, Wyatt PW, Hindson CM, Bharadwaj R, et al. 2017. Massively parallel digital transcriptional profiling of single cells *Nature Communications* **8**:14049. DOI: <https://doi.org/10.1038/ncomms14049>, PMID: 28091601
- Zhou Y**, Pernet V, Hauswirth WW, Di Polo A. 2005. Activation of the extracellular signal-regulated kinase 1/2 pathway by AAV gene transfer protects retinal ganglion cells in glaucoma *Molecular Therapy* **12**:402–412. DOI: <https://doi.org/10.1016/j.ymthe.2005.04.004>, PMID: 15975850